

# Salient Object Detection via Integrity Learning

Mingchen Zhuge<sup>†</sup>, Deng-Ping Fan<sup>†</sup>, Nian Liu, Dingwen Zhang,  
Dong Xu *Fellow, IEEE*, and Ling Shao *Fellow, IEEE*

**Abstract**—Although current salient object detection (SOD) works have achieved fantastic progress, they are cast into the shade when it comes to the integrity of the predicted salient regions. We define the concept of integrity at both the micro and macro level. Specifically, at the micro level, the model should highlight all parts that belong to a certain salient object, while at the macro level, the model needs to discover all salient objects from the given image scene. To facilitate integrity learning for salient object detection, we design a novel **Integrity Cognition Network (ICON)**, which explores three important components to learn strong integrity features. 1) Unlike the existing models that focus more on feature discriminability, we introduce a diverse feature aggregation (DFA) component to aggregate features with various receptive fields (*i.e.*, kernel shape and context) and increase the feature diversity. Such diversity is the foundation for mining the integral salient objects. 2) Based on the DFA features, we introduce the integrity channel enhancement (ICE) component with the goal of enhancing feature channels that highlight the integral salient objects (at both the micro and macro levels) while suppressing the other distracting ones. 3) After extracting the enhanced features, the part-whole verification (PWV) method is employed to determine whether the part and whole object features have strong agreement. Such part-whole agreements can further improve the micro-level integrity for each salient object. To demonstrate the effectiveness of ICON, comprehensive experiments are conducted on seven challenging benchmarks, where promising results are achieved. Codes and results are available at: <https://github.com/mczhuge/ICON>.

**Index Terms**—Saliency Detection, Salient Object Detection, Capsule Network, Integrity Learning.

## 1 INTRODUCTION

**S**ALIENT object detection (SOD) aims to imitate the human visual perception system to capture the most significant regions in a given image scene [1], [2], [3]. As SOD is widely used in the field of computer vision, it plays a vital role in many downstream tasks, such as object detection [4], image retrieval [5] and semantic segmentation [6], [7], [8].

Traditional SOD methods [1], [9] predict saliency maps in a bottom-up manner, and are mainly based on the handcrafted features, such as color contrast [10], [11], boundary background [12], [13], and center priors [14]. To improve the representation capacity of the features used in SOD, current models employ convolutional neural network (CNN) and fully convolutional network (FCN) architectures to enable powerful feature learning processes to replace manually designed features. These methods have achieved remarkable progress and pushed the performance of SOD to a new level. More details of recent deep learning based SOD methods can be found in the surveys/benchmarks in [1], [3], [15], [16], [17].

The current success in building deep learning based salient object detectors is mainly due to the consideration of *multi-scale/level feature aggregation, contextual modeling, top-down modeling, and edge-guided learning* mechanisms. Specifically,

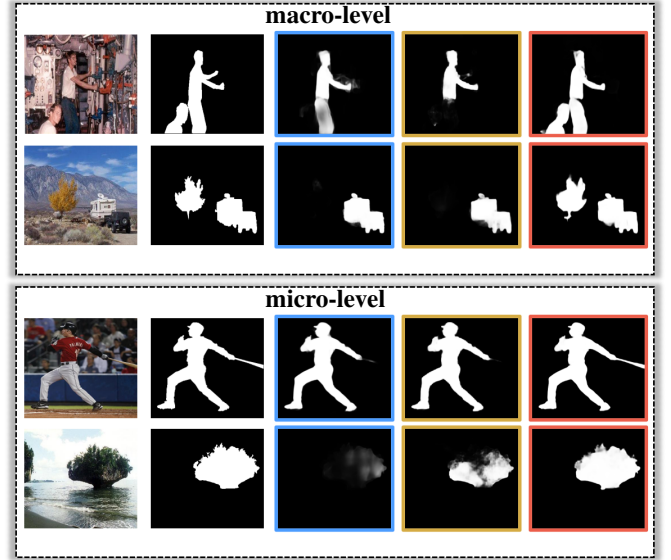


Fig. 1. Illustration of the integrity issue at both the macro and micro level. Compared with current state-of-the-art algorithms, our method can better detect salient regions integrally. The first two rows are the image and ground truth. Noted that: ■ EGNet [18], ■■ MINet [19], ■■■ Ours.

- <sup>†</sup>Equal contributions. Author ordering is random.
- Mingchen Zhuge is with the College of Computer Science, Chinese University of Geoscience, Wuhan, China. (Email: mczhuge@cug.edu.cn)
- Deng-Ping Fan, Nian Liu and Ling Shao are with the Inception Institute of Artificial Intelligence, Abu Dhabi, UAE. (Email: dengpingfan@mail.nankai.edu.cn, liunian228@gmail.com, ling.shao@inceptioniiai.org)
- Dingwen Zhang is with the Brain and Artificial Intelligence Laboratory, School of Automation, Northwestern Polytechnical University, Xi'an 710072, China. (Email: zhangdingwen2006yyy@gmail.com)
- Dong Xu is with School of Electrical and Information Engineering, The University of Sydney, Sydney, New South Wales Australia. (Email: dong.xu@sydney.edu.au)
- Corresponding author: Dingwen Zhang.

models with a multi-scale/level feature aggregation mechanism enhance the features from different levels and scales of the network and fuse them to generate the final salient object detection results. These approaches can help discover salient objects of various sizes and highlight the salient regions under the guidance of both coarse semantics and fine details. For example, the network proposed by Zhang *et al.* [20] first adaptively fuses multi-level features at five different scales and then generates the final saliency maps by integrating the results predicted at each feature scale. Similarly,

Luo *et al.* [21] proposed to extract the global and local features at the low and high feature scales, respectively, and then fuse them to generate the final saliency maps.

Contextual modeling is another key mechanism in salient object detection. It helps infer the saliency of each local region by considering the surrounding contextual information. Current studies in the field of SOD usually design various attention modules to explore such contextual information. Specifically, Zhao *et al.* [22] proposed the pyramid feature attention network, where channel attention and spatial attention modules are introduced to process high-level and low-level features, respectively, and consider the contextual information at different feature channels and spatial locations. Liu *et al.* [23], [24] proposed to learn pixel-wise contextual attention for salient object detection. Deep models learnt with such an attention module can infer the relevant importance between each pixel and its global/local context location and thus achieve the selective aggregation of contextual information.

For top-down modeling, some SOD methods adopt carefully designed decoding network streams to gradually infer salient regions under the guidance of high-level semantic cues. For example, Wang *et al.* [25] built an iterative and cooperative inference network for salient object detection, where multiple top-down network streams work cooperatively with the bottom-up network streams in an iterative inference manner. Zhao *et al.* [26] proposed a gated dual-branch decoding structure to build cooperation among different levels of features in the top-down flow, improving the discriminability of the whole network. In [27], Liu *et al.* adopted a pyramid pooling module to build global guiding features, which they introduced to improve the top-down flow modeling.

In order to produce accurate predictions of the salient object boundaries, another group of methods introduce additional network streams or learned objective functions to force the network to pay more attention to the contours that separate the salient objects from the surrounding background. For examples, Wei *et al.* [28] built a label decoupling framework for salient object detection, which explicitly decomposes the original saliency map into a body map and a details map. Specially, the body map concentrates on central areas of the salient objects, while the details map focuses on regions around the object boundaries. To improve the prediction precision of the salient contours and reduce the local noise in the salient edge prediction, Wu *et al.* [29] have proposed to facilitate the foreground contour and edge detection tasks guide each other in the mutual learning modules.

Although the aforementioned mechanisms can improve the salient object detection performance in terms of several aspects, the detection results produced are still not optimal. In our view, this is likely due to caused by the under-exploration of another helpful and important mechanism, *i.e.*, the *integrity learning* mechanism (see Figure 1). Specifically, we define the integrity learning mechanism at two levels. At the micro level, the model should focus on part-whole relevance within a single salient object. At the macro level, in contrast, the model needs to identify all salient objects within the given image scene.

In order to pursue two-level integrity, we introduce three key components in our deep neural network design. The first component is the diverse feature aggregation (DFA). Unlike existing models which focus more on feature discriminability, DFA aggregates the features from various receptive fields (in terms of both the kernel shape and context) to increase the feature diversity. Such feature diversity provides foundations for mining the integral salient objects, as it considers richer contextual patterns

to determine the activation of each neuron. The second component is called integrity channel enhancement (ICE), which aims at enhancing the feature channels that highlight the integral salient objects (at both the micro and macro levels) while suppressing the other distracting ones. As it is hard for the feature channels enhanced by ICE to perfectly match the real salient object regions, we further adopt a part-whole verification (PWV) component to judge whether the part features and whole features have strong agreement to form the integral objects. This can help further improve integral learning at the micro level.

It is worth mentioning that some existing works have also tried to solve the macro-level integrity issue by introducing the subtitizing task for learning deep salient object detectors [30], [31]. However, these methods require additional supervision information on the number of salient objects within each image. In contrast, our newly proposed approach can tackle both macro-level and micro-level integrity issues within a unified and entirely different learning framework, without any additional supervision information.

Our overall framework for integrity learning is called Integrity Cognition Network (ICON), details of which are shown in Fig. 2. Specifically, ICON first leverages five convolutional blocks for basic feature extraction. Then, it passes the deep feature of each level to a diverse feature aggregation module to extract the diverse feature bases. Next, the diverse feature bases extracted from three adjacent feature levels are sent to an integrity channel enhancement module, where an integrity guiding map is generated and then used to guide the attention weighting of each feature channel. Finally, the integrity channel enhancing features produced from the four feature levels are combined and passed through the part-whole verification module, which is implemented using the capsule routing layers [32]. After further verifying the agreements between the object parts and whole regions, the produced features are beneficial for dealing with cases of missing parts. To sum up, this paper has three main contributions:

- We study the integrity issue in SOD, which is an essential yet under-studied issue in this field.
- We introduce three important components for achieving integral SOD, namely diverse feature aggregation, integrity channel enhancement, and part-whole verification, respectively.
- We design a novel network, *i.e.*, ICON, that incorporates the three components and demonstrate its effectiveness on seven challenging datasets. In addition to its prominent performance, our approach also achieves real-time detection speed ( $\sim 56$  fps).

The remainder of the paper is organized as follows. In Section 2, we discuss the related works on boundary-oriented modeling and multi-scale feature learning for the SOD task. In Section 3, we describe the proposed ICON in detail. Experimental results, including a performance evaluation and comparison, are included in Section 4. Finally, conclusions are drawn in Section 5.

## 2 RELATED WORK

Over the past several decades, a number of SOD methods have been proposed and have achieved encouraging performance on various benchmark datasets. In addition to the approaches [33], [34], [35], [36], [37], [38], [39], [40], [41], [42], [43], [44] designed for processing single RGB images (the problem investigated in this work), several interesting works have also been

proposed for detecting salient objects from video sequences, image groups, multi-modal imaging data, or with very limited human annotation.

## 2.1 SOD from Video Sequences

Video salient object detection aims at detecting salient objects from an input video sequence. In video salient object detection, the salient objects from the whole video need to be identified and their motion is tracked to achieve pixel-wise segmentation in each video frame. To solve this problem, Wang *et al.* [45] proposed a short-term analysis method for video frames by directly learning temporal saliency patterns from the adjacent frame pairs. The deep model was built using a fully convolutional network architecture, while a synthetic data-based training scheme was adopted to address the insufficient training data issue. Shokri *et al.* [46] built a non-local deep network for video salient object detection, where the non-local attention mechanism is applied to capture the long-range dependencies for both appearance and motion features. In [47], Ren *et al.* introduced the curriculum learning mechanism into the learning process of their video salient object detector. By selectively extracting feature activations using the ground truth data, they were able to reduce learning ambiguities at the beginning of the training process. In [48], Su *et al.* studied how to better exploit the complementary spatial and temporal information for video salient object detection. To facilitate effective fusion of spatio-temporal information, they constructed a symmetric two-bypass network architecture and built the novel dynamic spatio-temporal network. Song *et al.* [49] combined pyramid dilated convolution with convolutional LSTM [50] to capture multi-scale spatiotemporal information for video salient object detection. We refer readers to recent benchmark work [51] for more details.

## 2.2 SOD from Image Groups

A recent research direction for the SOD community is to detect co-salient objects from multiple related images [52]. In this task, the saliency of the object within a specific image is influenced by those presented in the other images. To address this problem, Zhang *et al.* [53] proposed a unified co-saliency detection framework by exploring both the wide (visually similar images) and deep (high-level semantics) information. By modeling co-saliency detection as a weakly supervised classifier learning problem, Zhang *et al.* [54] established a self-paced multi-instance learning framework to produce the proper metrics to measure the intra-image contrast and the inter-image consistency in a self-learning way. In [55], Fan *et al.* collected the high-quality and large-scale CoSOD3k dataset to promote the development of co-saliency detection methods. In [56], Jiang *et al.* proposed a general optimization framework with adaptive graph learning for exploring both interactive information among different images and individual salient information within each image for co-saliency detection. In [57], Jin *et al.* built an intra-saliency correlation network for co-saliency detection, where the basic idea is to better exploit off-the-shelf single-image saliency cues to improve the co-saliency detection performance. Details of other state-of-the-art models can also be found in our recent work [58].

## 2.3 SOD from Multi-Modal Imaging Data

Another emerging trend in the SOD community is multi-modal saliency learning. In this research direction, the models need to

identify the salient objects from both an RGB image and another form of images captured by imaging equipment, such as the depth or infrared sensors. To tackle this problem, Han *et al.* [59] built an early deep model to transfer the structure of an RGB-based deep neural network to process depth view data and fuse the deep representations of both views to generate the final saliency prediction results. Zhang *et al.* [60] proposed a probabilistic RGB-D saliency detection network, which uses conditional variational autoencoders to model the prediction uncertainty and then fuses the saliency maps generated for each input image to produce the final prediction. In [61], Liu *et al.* proposed the self-mutual attention method for RGB-D saliency detection, where self-attention is first used to explore the contextual information within each modality of data. Then, mutual attention is further designed to facilitate communication between the two-modality data. Considering the non-ideal quality of the depth data, Zhang *et al.* [62] proposed to take into account both the global the location and local detail complementarities from the RGB and depth imaging data. They also designed a compensation-aware loss to further assist the network learning procedure. The complete history of multi-modal SOD can be found in the survey [63] and benchmark [2] works. In addition, light field SOD [64], [65] and high-resolution SOD [35], [66] are two potential directions in future research.

## 2.4 SOD with Limited Human Annotation

Besides purely pursuing high accuracy of detected saliency regions, another group of deep learning-based salient object detection methods focus more on the labor costs of collecting the manually labeled ground-truth data. For example, Zhang *et al.* [67], [68] learned a deep salient object detector under supervision formed by fusing different classic yet unsupervised saliency detection models. To build a more robust unsupervised mechanism, Nguyen *et al.* [69] further introduced a systematic curriculum to incrementally refine the pseudo-labels generated by the unsupervised saliency detection models. Zhang *et al.* [70] and Zhang *et al.* [71] proposed to model each noisy label generated by unsupervised handcrafted feature-based method as a sum of a clean saliency map and a noise map. The former is generated by a deep model, which is implicitly trained and finally used as the desired saliency model. In contrast, Li *et al.* [72] and Zeng *et al.* [73] proposed to leverage weak image-level supervision to train a deep salient object detector. Specifically, Li *et al.* [72] used a classification network to generate a coarse salient object activation map to help train the deep saliency network. Zeng *et al.* [73] enriched the weak supervision signals by additionally introducing image captions and unlabeled data to facilitate the training process. In [74], Zhang *et al.* leveraged scribble annotations as weak supervision signals to mitigate the labor of pixel-wise dense saliency labeling. More recently, Zhang *et al.* [75] designed an adversarial-paced learning model that can learn deep salient object detectors from a small portion of annotated training images.

## 3 FRAMEWORK

### 3.1 Overview of ICON

As shown in Fig. 2, our method is based on an encoder-decoder architecture. The encoder uses ResNet-50 as the backbone to extract multi-level features, while the decoder integrates these multi-level features and generates the saliency map with multi-layer supervision. For simplicity, from here on we denote the features generated

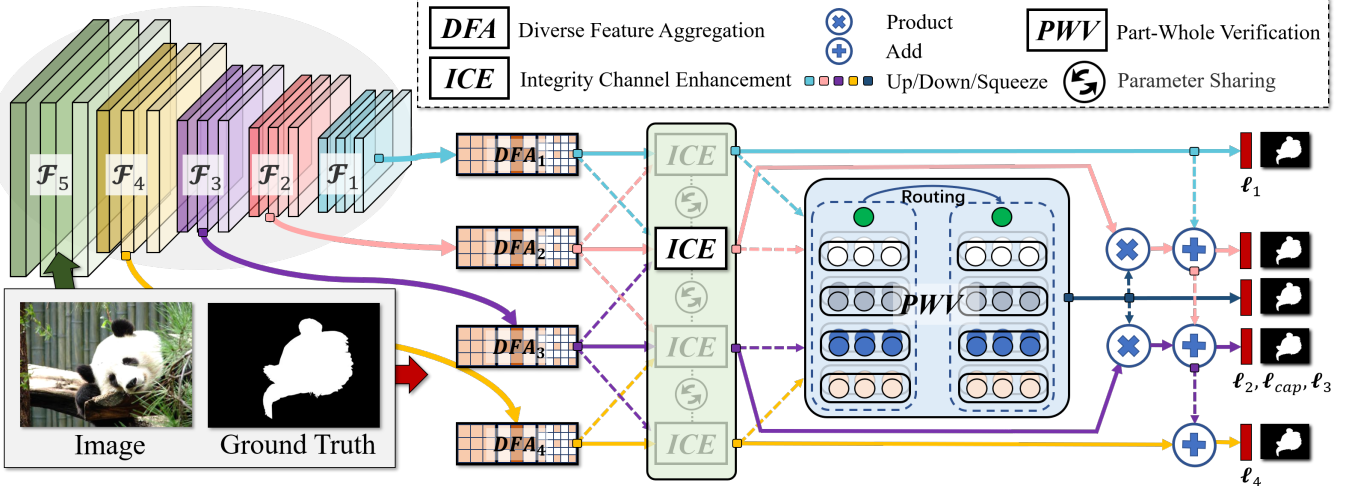


Fig. 2. The overall architecture of the proposed ICON. Feature extraction:  $\mathcal{F}_1$  -  $\mathcal{F}_5$  denote different layers from ResNet-50 [76]. Component 1: DFA aggregates the features with various receptive fields. Component 2: ICE aims at enhancing the feature channels that highlight the potential integral salient object. Component 3: PWV judges whether the part features and whole feature have strong agreement.  $\rightarrow$  indicates that features are transferred at the same level, while  $\dashrightarrow$  denotes cross-level feature flows.

by the backbone as a set  $\mathbf{F}_{bkb} = \{\mathbf{F}_{bkb}^{(1)}, \mathbf{F}_{bkb}^{(2)}, \mathbf{F}_{bkb}^{(3)}, \mathbf{F}_{bkb}^{(4)}, \mathbf{F}_{bkb}^{(5)}\}$ . To improve the computational efficiency, we do not use  $\mathbf{F}_{bkb}^{(1)}$  in the decoder due to its large spatial size.

Next, we enhance the backbone features by passing them through the diverse feature aggregation (DFA) module, which consists of diverse convolutional blocks. Thereafter, we further use the integrity channel enhancement (ICE) module to strengthen the responses of the integrity-related channels and coarsely highlight the integral salient parts. Finally, we utilize the part-whole verification (PWV) module to verify the agreement between object parts and the whole salient region, to further refine the saliency map.

### 3.2 Diverse Feature Aggregation

We adopt DFA to enhance the diversity of the extracted multi-level features, using three kinds of convolutional blocks with different kernel sizes and shapes, as shown in Fig. 3-(A). Technically, we utilize a practical combination of the asymmetric convolution [77], atrous convolution [78], and the original convolution to capture diverse spatial features. The whole procedure is summarized as follows:

$$\mathbf{F}_{dfa}^{(i)} = [\mathbf{X}_{asy} \parallel \mathbf{X}_{atr}^2 \parallel \mathbf{X}_{ori}] (\mathbf{F}_{bkb}^{(i)}), \quad (1)$$

where  $\mathbf{F}_{dfa}^{(i)}$  denotes the features produced from the above process,  $\mathbf{X}_*$  denotes different types of convolution blocks(asymmetric, atrous, original), and  $\parallel$  is the concatenation operation.

Note that we use  $\mathbf{X}_{atr}^r$  to denote atrous convolution operations with different dilation rates  $r^1$ , and use the asymmetric convolution ( $\mathbf{X}_{asy}$ ) with a crux-shape [77], which contains three convolution layers with a normal square  $3 \times 3$  kernel  $K^{[1]}$ , a horizontal  $1 \times 3$  kernel  $K^{[2]}$ , and a vertical  $3 \times 1$  kernel  $K^{[3]}$ , shared in the same sliding window. It can be described as:

$$\mathbf{X}_{asy} = \mathbf{I} \star (K^{[1]} \oplus K^{[2]} \oplus K^{[3]}), \quad (2)$$

where  $\star$  is the 2D convolution operator and  $\mathbf{I}$  denotes the input feature.

1. e.g.,  $\mathbf{X}_{atr}^2$  means the atrous convolution with dilation rate 2.

In such a way, our DFA module can enrich the feature space by fusing the knowledge learned from the crux kernel, dilated kernel, and normal kernel in the first stage. Besides, pyramid-based atrous convolutions can further enlarge the receptive field in the second portion. As a result, DFA can cover different salient regions in various contexts, enhancing integrity. We mark the features processed by DFA as  $\mathbf{F}_{dfa} = \{\mathbf{F}_{dfa}^{(2)}, \mathbf{F}_{dfa}^{(3)}, \mathbf{F}_{dfa}^{(4)}, \mathbf{F}_{dfa}^{(5)}\}$ .

### 3.3 Integrity Channel Enhancement

Several recent studies [79], [80], [81] have presented promising results on visual categorization using the spatial or channel attention mechanism. Though these methods are driven by various motivations, they can be thought of as building correspondence across different features to highlight the most significant parts. However, none of the previous works considers mining integrity information with the attention models. From this perspective, we propose the ICE module to further mine the relations within different channels and enhance the channels that highlight the potential integral targets.

We consider multi-scale information from every three adjacent feature levels and use ICE to fuse them. Concretely, for each feature level with a size of  $C \times H \times W$ , we also consider its next and previous feature levels and use up-sampling and down-sampling operators to scale them to the spatial size of  $H \times W$ , respectively. After that, we build the proposed ICE module by following the query-key-value attention mechanism [82]. We first generate query, key, and value features by aggregating the three input features using three different aggregation schemes, *i.e.*, concatenation, element-wise addition, and element-wise multiplication, respectively, to enhance the feature diversity. Then, three  $3 \times 3$  convolutional layers are used to generate three fused feature maps  $\mathbf{Q}'$ ,  $\mathbf{K}$ , and  $\mathbf{V}$ , among which the last two are referred to as the key feature and the value feature, respectively, as shown in Fig. 3-(B).

Next, we generate the query feature  $\mathbf{Q}$  based on the initial feature  $\mathbf{Q}'$ . We first calculate the  $l_2$  norm of each channel on  $\mathbf{Q}'$ , to squash its spatial size to 1. Then, we use a fully connected (FC) layer to linearly transform it to  $C$  channels and perform Softmax normalization to produce a channel attention map with

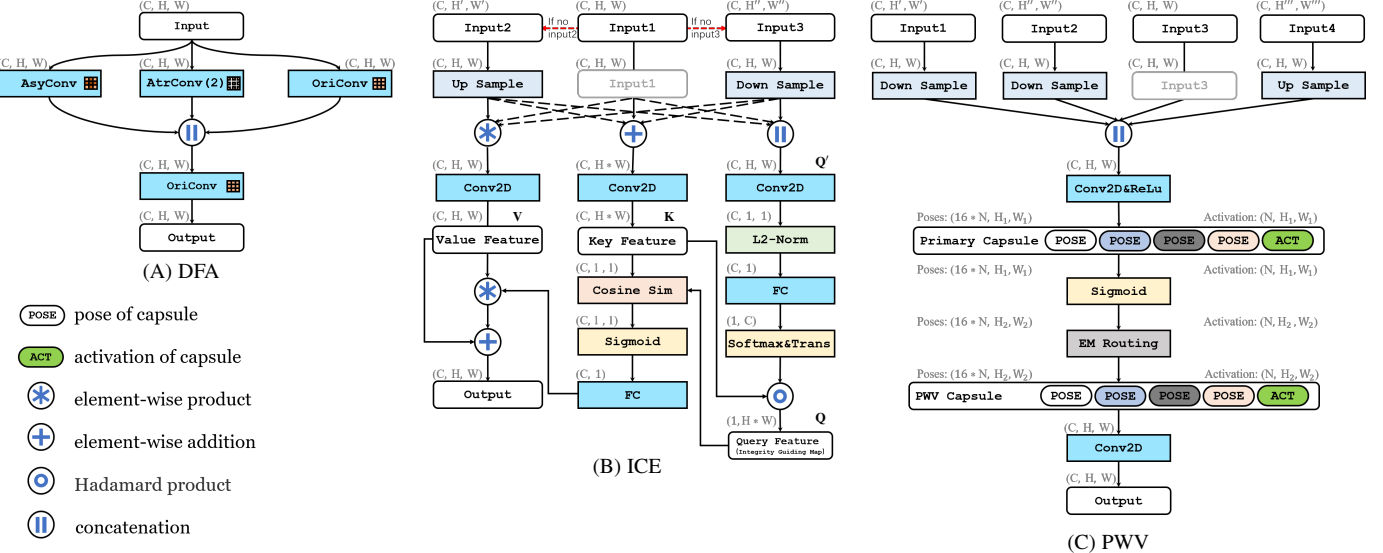


Fig. 3. Details of the proposed modules. (A) The diverse feature aggregation component, which mixes different convolutional kernels to enhance the representational ability of framework. (B) The Integrity Channel Enhancement component, which mines integrity information on channels. (C) The Part-Whole Verification component designed for modeling the relation between parts and whole. Cosine Sim = cosine similarity, AsyConv = asymmetric convolution block, AtrConv = atrous convolution block, OriConv = Conv2D, EM Routing = the Expectation-Maximum routing mechanism. C, H, W denote the number of channels, the height, and the width of the feature tensor, respectively.

a size of  $C \times 1$ . Next, we transpose it and multiply it by  $\mathbf{K}$  using the Hadamard product  $\circ$  to generate the query feature. The whole process can be formulated as follows:

$$\mathbf{Q} = \text{Softmax}(\text{FC}(\text{Norm}(\mathbf{Q}'))^\top \circ \mathbf{K}, \quad (3)$$

where the final query feature is  $\mathbf{Q} \in \mathbb{R}^{1 \times H \times W}$ , which encodes the integrity guiding map by using channel attention to aggregate all channels of  $\mathbf{K}$ .

Then, we compute the cosine similarity between  $\mathbf{Q}$  and each channel of  $\mathbf{K}$ , to produce a similarity vector with a size of  $C \times 1$ , which measures how accurately each channel of  $\mathbf{K}$  learns the integrity. A Sigmoid activation function and an FC layer are further used to transform the similarity vector to an integrity channel attention vector  $\mathbf{a} \in \mathbb{R}^{C \times 1}$ . This process can be represented as:

$$\mathbf{a} = \text{FC}(\text{Sigmoid}(\text{Sim}(\mathbf{Q}, \mathbf{K}))), \quad (4)$$

where  $\mathbf{a}$  generates large attention weights for the channels in order to highlight the integral targets.

Finally, we use  $\mathbf{a}$  to weight different channels of  $\mathbf{V}$  for channel enhancement. A residual connection is also used to help better train the network. Namely, the output feature is produced by  $\mathbf{O} \in \mathbb{R}^{C \times H \times W}$ :

$$\mathbf{O} = \mathbf{V} + \mathbf{A} * \mathbf{V}, \quad (5)$$

where  $\mathbf{A}$  is obtained by expanding the spatial dimension of  $\mathbf{a}$  to  $W \times H$  and  $*$  denotes an element-wise product.

By using the proposed ICE module, the channels with better integrity can be effectively enhanced. As can be seen in Fig. 4, the features produced by ICE tend to highlight integral objects at both micro and macro level. In our implementation, if there are not enough multi-level features input in the first and the last level, we fill the input with the feature from the current level.

### 3.4 Part-Whole Verification

The PWV module aims to enhance the learned integrity features by measuring the agreement between object parts and the whole

salient region. To achieve this goal, we adopt the capsule network [32], [83], which has proven effective in modeling part-whole relationships. Learning from the success of the prior work SegCaps [84], we embed a capsule network into ICON. The inputs of our PWV are four different ICE features ( $\mathbf{F}_{ice}^i$ ). Specifically, we first reduce the ICE features at each level to a united resolution, *i.e.*,  $22 \times 22$ , in order to reduce computational costs. Then, we concatenate all the features and pass them to a 2D convolutional layer.

Next, we build our primary capsules. To be specific, we use eight pose vectors to build a pose matrix  $\mathbf{M}$  and activation  $\phi \in [0, 1]$  to represent each capsule. The pose matrix contains the instantiated parameters to reflect the properties of object parts or the whole object, while the activation represents the existence probability of the object. Capsules from the primary capsule layer pass information to those in the next PWV capsule layer through a routing-by-agreement mechanism. Specifically, when the capsules from a lower-layer produce votes for the capsules in a higher-level, the votes  $\omega_{ij}$  are obtained by a matrix multiplication operation between the learned transformation matrices  $\mathbf{T}_{ij}$  and the lower level pose matrix  $\mathbf{M}_i$ , where  $i$  and  $j$  are the indices of the lower- and higher-level capsules, respectively. Once these votes are obtained, they are used in the EM routing algorithm [32] to get the higher level capsule  $\mathbf{C}_j$  with the pose matrices  $\mathbf{M}_j$  and activation  $\phi_j$ . After that, we obtain the part-whole verified features. Finally, we re-scale these features to the size at each feature level and perform the multiply them by the original ICE features.

### 3.5 Feature Fusion and Supervision Strategy

In our ICON, we use an element-wise product to fuse the middle two features generated by ICE with the part-whole verified feature generated by PWV. Subsequently, element-wise addition and up-sampling operations are introduced to fuse the features at adjacent levels in a bottom-up manner, which encourages the cooperation among multi-scale features. In this work, in addition to the BCE loss, we also integrate the IoU loss driving the training process

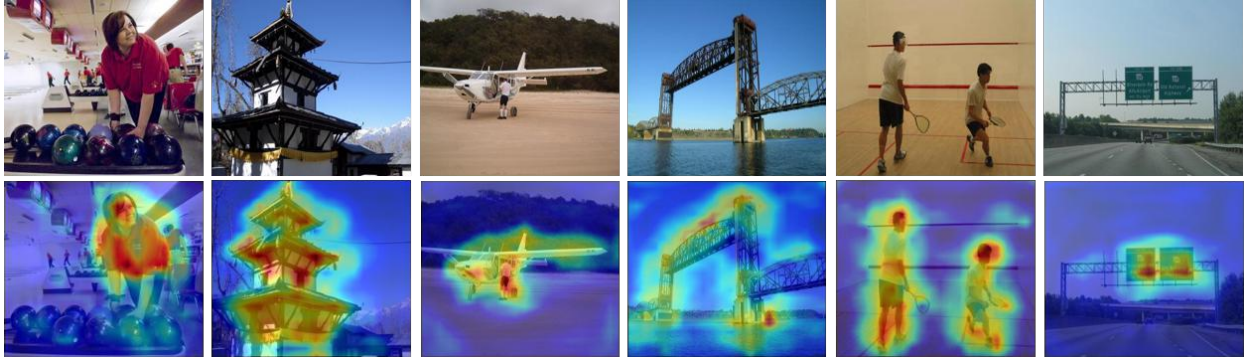


Fig. 4. Several feature heatmaps after passing through ICE. The ICE module helps our framework to focus on the integral salient regions.

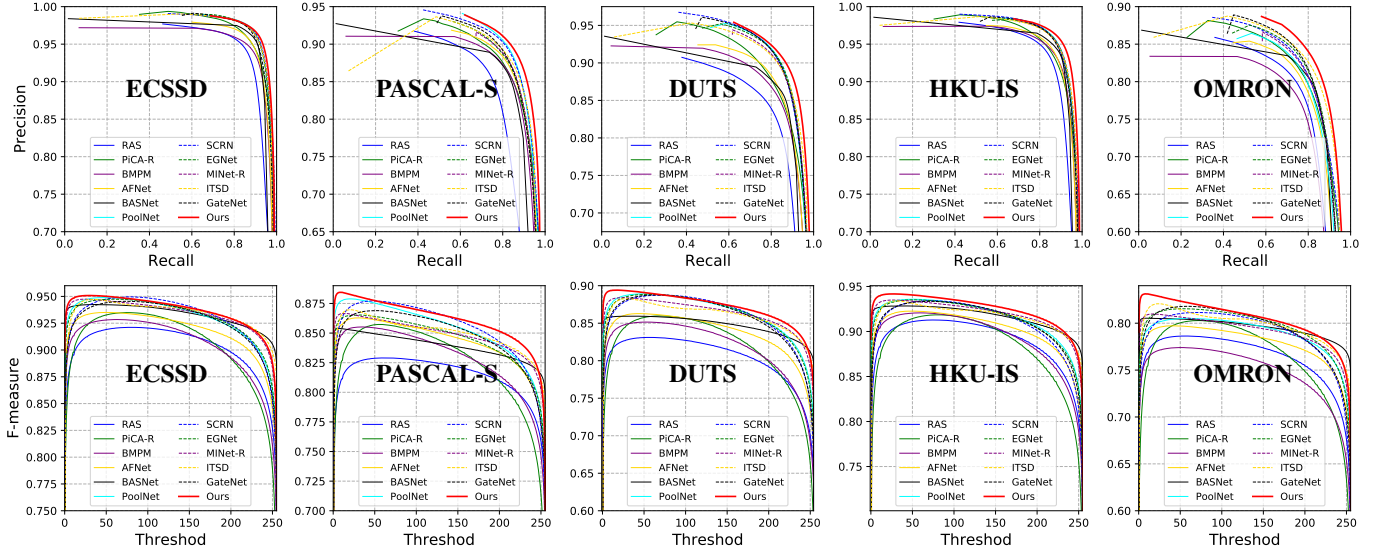


Fig. 5. Precision-recall curves and F-measure curves of the proposed method and other SOTA algorithms on five popular SOD datasets.

to consider global context [85]. Specifically, the overall loss  $L$  of the proposed ICON is formulated as  $L_{cpr}(P, G)$ , where  $P$  is the generated saliency prediction map, and  $G$  is the ground truth saliency map.  $L_{cpr}$  incorporates the cooperative BCE loss and IoU loss, *i.e.*,  $L_{cpr} = L_{bce} + L_{iou}$ , where  $L_{bce}$  is formulated as follows:

$$L_{bce} = - \sum_{(x,y) \in P, G} [G(x,y) \log(P(x,y)) + (1 - G(x,y)) \log(1 - P(x,y))], \quad (6)$$

while  $L_{iou}$  is defined as:

$$L_{iou} = 1 - \frac{\sum_{x=1}^H \sum_{y=1}^W P(x,y)G(x,y)}{\sum_{x=1}^H \sum_{y=1}^W [P(x,y) + G(x,y) - P(x,y)G(x,y)]}, \quad (7)$$

where  $G(x,y)$  is the ground truth label of the location  $(x,y)$  and  $P(x,y)$  is the predicted saliency probability.

The cooperative loss can guide our ICON to obtain high-quality regional segmentation and clear boundaries. The BCE loss is utilized to maintain a smooth gradient for all pixels, while the IoU loss can help enhance the learning process to increase the confidence of foreground predictions.

## 4 EXPERIMENTS

### 4.1 Datasets

We train our ICON on the **DUTS-TR** [86] dataset, which is commonly used for the SOD task and contains 10,553 images. Then, we evaluate our model on seven popular benchmarks: **ECSSD** [87], **HKU-IS** [88], **DUT-OMRON** [12], **PASCAL-S** [89], **DUTS-TE** [86], **SOD** [90] and attribute-based **SOC** [15], which are all annotated with pixel-level labels. Specifically, ECSSD is made up of 1,000 images with meaningful semantics. HKU-IS includes 4,447 images, which contain multiple foreground objects. DUT-OMRON consists of 5,168 images with at least one object. These objects are usually structurally complex. PASCAL-S was built from a dataset originally used for semantic segmentation, and it consists of 850 challenging images. DUTS is a relatively large salient object detection dataset with two subsets. The 10,553 images in DUT-TR are used for training, and the 5,019 images in DUT-TE are employed for testing. SOD includes 300 very challenging images. SOC contains complicated scenarios, which are more challenging than those in the above six SOD datasets.

### 4.2 Implementation Details

We run all experiments on the publicly available Pytorch 1.5.0 platform. An eight-core PC with Intel Core i7-9700K CPU (with

TABLE 1

Quantitative results on different datasets, including ECSSD, PASCAL-S, DUTS, HKU-IS, DUT-OMRON, SOD. The best and second best results are highlighted in **Red** / **Blue**.  $E_\phi$  denotes adaptive E-measure [93]. Symbols “↑”/“↓” mean that a higher/lower score is better.

Dataset	Metric	2018				2019~2020										ICON Ours		
		BMPM [94]	PiCAR-R [23]	R3Net [95]	RAS [96]	PAGE [97]	AFNet [98]	BASNet [85]	CPD-R [99]	PoolNet [27]	SIBA [100]	EGNet [18]	SCRN [101]	F3Net [102]	MINet [19]	ITSD [103]	GateNet [104]	
ECSSD [87]	$S_m \uparrow$	0.911	0.917	0.910	0.893	0.912	0.913	0.916	0.918	0.926	0.924	0.925	<b>0.927</b>	0.924	0.925	0.925	0.920	<b>0.931</b>
	$E_\xi \uparrow$	0.914	0.913	0.929	0.914	0.920	0.918	0.921	0.925	0.925	<b>0.928</b>	<b>0.927</b>	0.926	0.925	<b>0.927</b>	<b>0.927</b>	0.924	0.924
	$F_\beta^w \uparrow$	0.871	0.867	0.902	0.857	0.886	0.886	0.904	0.898	0.904	0.908	0.903	0.900	<b>0.912</b>	0.911	0.910	0.894	<b>0.920</b>
	$MAE \downarrow$	0.045	0.046	0.040	0.056	0.042	0.042	0.037	0.037	0.035	0.035	0.037	0.037	0.034	<b>0.033</b>	0.034	0.040	<b>0.031</b>
PASCAL-S [89]	$S_m \uparrow$	0.843	0.848	0.800	0.792	0.835	0.848	0.832	0.842	0.858	0.845	0.846	<b>0.863</b>	0.854	0.850	0.853	0.851	<b>0.864</b>
	$E_\xi \uparrow$	0.841	0.832	0.836	0.829	0.841	0.850	0.846	0.849	0.852	0.852	0.848	<b>0.857</b>	<b>0.859</b>	0.851	0.850	0.851	0.853
	$F_\beta^w \uparrow$	0.778	0.772	0.755	0.731	0.783	0.797	0.793	0.794	0.809	0.802	0.795	0.807	<b>0.816</b>	0.809	0.812	0.797	<b>0.830</b>
	$MAE \downarrow$	0.074	0.074	0.092	0.101	0.075	0.070	0.075	0.070	0.064	0.069	0.073	0.062	<b>0.061</b>	0.063	0.065	0.067	<b>0.059</b>
DUTS [86]	$S_m \uparrow$	0.862	0.869	-	0.839	0.854	0.867	0.866	0.869	0.886	0.879	0.887	0.885	<b>0.888</b>	0.884	0.885	0.885	<b>0.892</b>
	$E_\xi \uparrow$	0.860	0.862	-	0.861	0.869	0.879	0.884	0.886	0.896	0.892	0.891	0.888	<b>0.902</b>	0.898	0.895	0.889	<b>0.900</b>
	$F_\beta^w \uparrow$	0.761	0.754	-	0.740	0.769	0.785	0.803	0.795	0.817	0.811	0.815	0.803	<b>0.835</b>	0.825	0.823	0.809	<b>0.839</b>
	$MAE \downarrow$	0.049	0.043	-	0.059	0.052	0.046	0.048	0.043	<b>0.037</b>	0.040	0.039	0.040	<b>0.035</b>	<b>0.037</b>	0.041	0.040	<b>0.037</b>
HKU-IS [88]	$S_m \uparrow$	0.907	0.904	0.895	0.887	0.903	0.905	0.909	0.905	<b>0.919</b>	0.913	0.918	0.916	0.917	<b>0.919</b>	0.917	0.915	<b>0.925</b>
	$E_\xi \uparrow$	0.937	0.936	0.939	0.929	0.940	0.942	0.946	0.944	<b>0.953</b>	0.950	0.950	0.949	<b>0.953</b>	<b>0.953</b>	0.952	0.949	<b>0.956</b>
	$F_\beta^w \uparrow$	0.859	0.840	0.877	0.843	0.866	0.869	0.889	0.875	0.888	0.886	0.887	0.876	<b>0.900</b>	0.897	0.894	0.880	<b>0.908</b>
	$MAE \downarrow$	0.039	0.043	0.036	0.045	0.037	0.036	0.032	0.034	0.030	0.032	0.031	0.034	<b>0.028</b>	0.029	0.031	0.033	<b>0.027</b>
OMRON [12]	$S_m \uparrow$	0.809	0.832	0.815	0.814	0.824	0.826	0.836	0.825	0.831	0.832	<b>0.841</b>	0.837	0.838	0.833	0.840	0.838	<b>0.845</b>
	$E_\xi \uparrow$	0.837	0.841	0.850	0.846	0.853	0.853	0.869	0.866	0.868	0.860	<b>0.867</b>	0.863	<b>0.870</b>	0.865	0.863	0.862	0.866
	$F_\beta^w \uparrow$	0.681	0.695	0.728	0.695	0.722	0.717	<b>0.751</b>	0.719	0.725	0.736	0.738	0.720	0.747	0.738	0.750	0.729	<b>0.762</b>
	$MAE \downarrow$	0.064	0.065	0.062	0.062	0.062	0.057	0.056	<b>0.054</b>	0.059	<b>0.053</b>	0.056	<b>0.053</b>	0.055	0.061	0.055	0.058	
SOD [90]	$S_m \uparrow$	0.783	0.787	0.755	0.761	0.769	-	0.766	0.765	0.785	0.788	0.800	-	0.793	-	<b>0.803</b>	-	<b>0.818</b>
	$E_\xi \uparrow$	0.797	0.794	0.796	0.797	0.795	-	0.773	0.789	0.803	0.809	<b>0.816</b>	-	<b>0.812</b>	-	0.799	-	<b>0.812</b>
	$F_\beta^w \uparrow$	0.725	0.722	0.732	0.718	0.721	-	0.728	0.713	0.746	0.765	0.767	-	0.763	-	<b>0.777</b>	-	<b>0.791</b>
	$MAE \downarrow$	0.106	0.102	0.123	0.123	0.110	-	0.112	0.109	0.103	0.104	0.097	-	0.095	-	<b>0.093</b>	-	<b>0.081</b>

4.9GHz Turbo boost), 16GB 3000 MHz RAM and an RTX 2080Ti GPU card (with 11GB memory) is used for both training and testing. During network training, each image is first resized to 352×352 and data augmentation methods, such as normalizing, cropping and flipping, are used. Some of the encoder parameters are initialized from the ResNet-50 model [76]. We initialize some layers of PWV by zeros or ones, and other convolutional layers are initialized by [91]. We use the SGD optimizer [92] to train our network and its hyperparameters are set as: initial learning rate lr = 0.05, momen = 0.9, eps = 1e-8, weight\_decay = 5e-4. Warm-up and linear decay strategies are used to adjust the learning rate. The batch size is set to 32 and the maximum number of epochs is set to 48 (takes ~115 minutes). In addition, we use apex and fp16 to accelerate the training process. Gradient clipping is also used to prevent gradient explosion. The inference process for a 352×352 image only takes 0.0177s (~56 fps), including the IO time.

### 4.3 Evaluation Metrics

We use five metrics to evaluate our model and existing state-of-the-art algorithms:

(1) **MAE** evaluates the average pixel-wise difference between the predicted saliency map and the ground truth map. Let  $P$  and  $G$  denote the saliency map and the ground truth, which are normalized to [0, 1], respectively. We compute the MAE score by:

$$MAE = \frac{1}{W \times H} \sum_{x=1}^W \sum_{y=1}^H |P(x, y) - G(x, y)|, \quad (8)$$

where  $W$  and  $H$  are the width and height of images, respectively.

(2) **Weighted F-measure** ( $F_\beta^\omega$ ) [105] offers an intuitive generalization of  $F_\beta$ , and is defined as:

$$F_\beta^\omega = \frac{(1 + \beta^2) \text{Precision}^\omega \cdot \text{Recall}^\omega}{\beta^2 \cdot \text{Precision}^\omega + \text{Recall}^\omega}. \quad (9)$$

As adopted in [15], [20], [35], [106], [107], [108], [109], [110], [111], [112],  $F_\beta^\omega$  can handle the interpolation, dependency and equal-importance issues which might cause inaccurate evaluation by MAE and F-measure. Where  $\beta^2$  is set to 0.3 to emphasize the precision over recall, as suggested in the previous work [1]. By assigning different weights ( $\omega$ ) to different errors according to the specific location and neighborhood information,  $F_\beta^\omega$  extends TP, TN, FP, FN to non-binary values.

(3) **S-measure** ( $S_m$ ) [113] focuses on evaluating the structural similarity, which is much closer to human visual perception. It is computed as:

$$S_m = ms_o + (1 - m)s_r, \quad (10)$$

where  $s_o$  and  $s_r$  denote the region-aware and object-aware structural similarity and MAE is set as 0.5 according to [113].

(4) **E-measure** ( $E_\xi$ ) [93] combines the local pixel values with the image-level mean value in one term. It jointly captures image-level statistics and local pixel matching information, and can be computed as:

$$E_\xi = \frac{1}{W \times H} \sum_{x=1}^W \sum_{y=1}^H \theta(\xi), \quad (11)$$

where  $\xi$  is the alignment matrix and  $\theta(\xi)$  indicates the enhanced alignment matrix.

(5) **FNR** is the False Negative Ratio. According to our *integrity* thinking, we further evaluate the integrity using this metric. It can

TABLE 2

False negative ratios (FNRs) of our method and the baseline methods on ECSSD, PASCAL-S, DUTS, HKU-IS, DUT-OMRON, SOD. The best and second best results are highlighted in **Red** / **Blue**. Symbols “↑”/“↓” indicate that a higher/lower score is better results.

Dataset	Metric	2018					2019~2020										ICON Ours	
		BMPM [94]	PiCA-R [23]	R3Net [95]	RAS [96]	PAGE [97]	AFNet [98]	BASNet [85]	CPD-R [85]	PoolNet [27]	SIBA [100]	EGNet [18]	SCRN [101]	F3Net [102]	MINet [19]	ITSD [103]	GateNet [104]	
ECSSD [87]	<i>FNR</i> ↓	10.737	9.617	9.498	11.658	8.143	8.579	12.327	7.676	7.364	7.398	7.607	8.219	8.155	<b>6.699</b>	10.344	8.701	<b>6.558</b>
PASCAL-S [89]	<i>FNR</i> ↓	16.988	15.182	19.275	21.580	12.791	12.872	18.539	13.036	<b>11.709</b>	12.199	12.918	12.576	11.942	11.823	15.464	13.990	<b>10.099</b>
DUTS [86]	<i>FNR</i> ↓	11.109	9.475	-	12.831	10.392	10.168	14.137	10.711	8.660	8.706	<b>8.506</b>	9.083	9.019	8.713	10.858	9.085	<b>7.842</b>
HKU-IS [88]	<i>FNR</i> ↓	7.566	7.242	9.235	10.900	7.808	7.891	9.307	8.348	<b>6.437</b>	7.424	6.735	7.018	6.899	6.602	7.526	7.488	<b>5.611</b>
OMRON [12]	<i>FNR</i> ↓	17.713	<b>12.303</b>	14.993	17.228	13.237	15.207	16.414	16.188	14.722	12.372	13.200	13.320	14.573	13.511	12.474	13.500	<b>11.042</b>
SOD [90]	<i>FNR</i> ↓	30.810	29.001	32.980	30.797	28.249	-	35.682	29.917	28.130	27.065	<b>26.258</b>	-	-	-	30.754	-	<b>26.100</b>

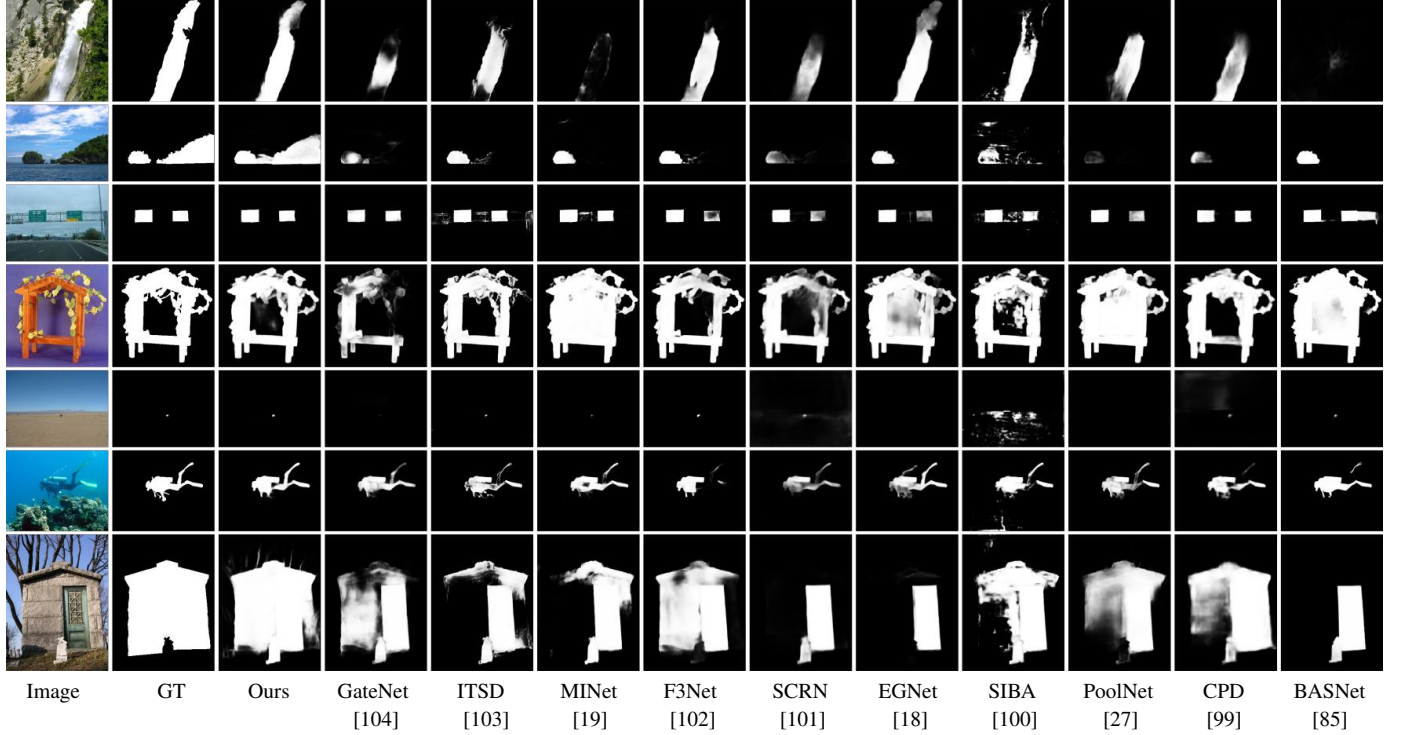


Fig. 6. Qualitative comparison of our method versus ten state-of-the-art methods. Unlike other models, our method not only locates the salient object accurately, but it also produces sharper edges with fewer background distractors in various scenarios.

detect whether the predictions are integral with salient pixels. The FNR is computed by:

$$FNR = \frac{1}{W \times H} \sum_{x=1}^W \sum_{y=1}^H FN(x, y). \quad (12)$$

We show several examples of FNR in Fig. 7. FNR clearly accurately reflects the *integrity* of predictions and is sensitive at both a macro and micro level.

#### 4.4 Comparison with the SOTAs

We compare our proposed approach with 16 very recent state-of-the-art SOD methods, including BMPM [114], PiCANet [23], R3Net [95], RAS [96], PAGE [97], AFNet [98], BASNet [85], CPD [99], PoolNet [27], SIBA [100], EGNet [18], SCRN [101], F3Net [102], MINet [19], ITSD [103] and GateNet [104]. For fair comparison, we use the saliency maps provided by the authors.

##### 4.4.1 Quantitative Evaluation

Table 1 reports the quantitative results on six traditional benchmark datasets, comparing with 16 state-of-the-art algorithms in

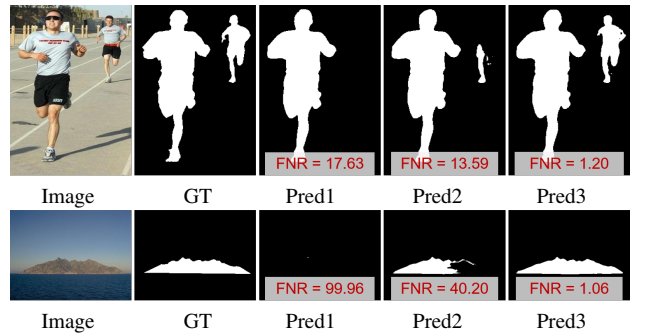


Fig. 7. Sample prediction results at different false negative ratios (FNR), where FNR heavily reflects the *integrity*.

terms of F-measure, weighted F-measure, MAE, S-measure and E-measure. Our model is clearly superior to other state-of-the-art alternatives. Besides, we also show the FNR results of ours and the baseline methods in Table 2. As can be seen, the proposed approach achieves the lowest FNR scores across all the datasets.

TABLE 3

Comparison of the proposed method with other SOTA models on the SOC test set. For  $\uparrow$  and  $\downarrow$ , the higher and lower scores indicate better result, respectively.  $E_\phi$  denotes adaptive E-measure [93]. The best and second best results are highlighted in **Red** / **Blue**.  $\dagger$  indicates that the results with parameters trained on SOC train set.

Attr	Metrics	Amulet [20]	DSS [115]	NLDF [116]	C2SNet [107]	SRM [117]	R3Net [95]	BMPM [94]	DGRL [118]	PiCA-R [23]	RANet [119]	AFNet [98]	CPD [99]	PoolNet [27]	EGNet [18]	SIBA [100]	SCRN [101]	ICON (Ours)
AC	$S_m \uparrow$	0.752	0.753	0.737	0.755	0.791	0.713	0.780	0.790	0.792	0.708	0.796	0.799	0.795	0.806	0.806	0.809	<b>0.832/0.840</b> $\dagger$
	$E_\phi \uparrow$	0.769	0.789	0.783	0.815	0.833	0.758	0.812	0.836	0.820	0.772	0.836	0.828	0.826	0.824	0.841	0.846	<b>0.855/0.867</b> $\dagger$
	$F_\beta^w \uparrow$	0.620	0.629	0.620	0.647	0.690	0.593	0.680	0.718	0.682	0.603	0.712	0.727	0.713	0.731	0.740	0.724	<b>0.767/0.778</b> $\dagger$
	$MAE \downarrow$	0.120	0.113	0.119	0.109	0.096	0.135	0.098	0.081	0.093	0.132	0.084	0.083	0.094	0.085	0.086	0.078	<b>0.066/0.062</b> $\dagger$
BO	$S_m \uparrow$	0.574	0.561	0.568	0.654	0.614	0.437	0.604	0.684	<b>0.729</b>	0.421	0.658	0.647	0.561	0.528	0.645	0.698	<b>0.752/0.702</b> $\dagger$
	$E_\phi \uparrow$	0.353	0.460	0.488	0.420	<b>0.442</b>	0.398	0.358	0.389	0.368	0.404	0.398	0.400	0.397	<b>0.443</b>	0.424	0.435	0.393/0.318 $\dagger$
	$F_\beta^w \uparrow$	0.612	0.614	0.622	0.730	0.667	0.456	0.670	0.786	<b>0.799</b>	0.453	0.741	0.739	0.610	0.585	0.720	0.778	<b>0.842/0.763</b> $\dagger$
	$MAE \downarrow$	0.346	0.356	0.354	0.267	0.306	0.445	0.303	0.215	<b>0.200</b>	0.454	0.245	0.257	0.353	0.373	0.271	0.224	<b>0.165/0.216</b> $\dagger$
CL	$S_m \uparrow$	0.763	0.722	0.713	0.742	0.759	0.659	0.761	0.770	0.787	0.624	0.768	0.773	0.760	0.757	0.784	<b>0.795</b>	0.792/0.845 $\dagger$
	$E_\phi \uparrow$	0.748	0.770	0.761	0.736	0.773	0.727	0.761	0.762	0.746	0.727	0.759	0.780	0.768	0.754	0.762	<b>0.782</b>	0.764/0.834 $\dagger$
	$F_\beta^w \uparrow$	0.663	0.617	0.614	0.655	0.665	0.546	0.678	0.714	0.692	0.542	0.696	0.724	0.681	0.677	0.726	0.717	<b>0.733/0.803</b> $\dagger$
	$MAE \downarrow$	0.141	0.153	0.159	0.144	0.134	0.182	0.123	0.119	0.123	0.188	0.119	0.114	0.134	0.139	0.117	<b>0.113</b>	<b>0.113/0.080</b> $\dagger$
HO	$S_m \uparrow$	0.791	0.767	0.755	0.768	0.794	0.740	0.781	0.791	0.809	0.713	0.798	0.803	0.815	0.802	0.819	0.823	<b>0.826/0.841</b> $\dagger$
	$E_\phi \uparrow$	0.809	0.807	0.799	0.785	0.815	0.794	0.806	0.805	0.791	0.783	0.813	0.830	0.836	0.816	<b>0.838</b>	0.830	0.825/0.864 $\dagger$
	$F_\beta^w \uparrow$	0.688	0.660	0.661	0.668	0.696	0.633	0.684	0.722	0.704	0.626	0.722	0.751	0.739	0.720	0.754	0.743	<b>0.763/0.785</b> $\dagger$
	$MAE \downarrow$	0.119	0.124	0.126	0.123	0.115	0.136	0.116	0.104	0.108	0.143	0.103	0.097	0.100	0.106	0.094	0.096	<b>0.091/0.078</b> $\dagger$
MB	$S_m \uparrow$	0.712	0.719	0.685	0.720	0.742	0.657	0.762	0.744	0.775	0.696	0.734	0.754	0.751	0.762	0.764	<b>0.792</b>	0.783/0.820 $\dagger$
	$E_\phi \uparrow$	0.732	0.751	0.737	0.768	0.762	0.687	0.784	0.788	0.758	0.744	0.760	0.786	0.770	0.776	<b>0.800</b>	<b>0.800</b>	0.774/0.799 $\dagger$
	$F_\beta^w \uparrow$	0.561	0.577	0.551	0.593	0.619	0.489	0.651	0.655	0.637	0.576	0.626	0.679	0.642	0.649	0.672	0.690	<b>0.697/0.746</b> $\dagger$
	$MAE \downarrow$	0.142	0.132	0.138	0.128	0.115	0.160	0.105	0.113	0.099	0.139	0.111	0.106	0.121	0.109	0.104	0.100	<b>0.095/0.072</b> $\dagger$
OC	$S_m \uparrow$	0.735	0.718	0.709	0.738	0.749	0.653	0.752	0.747	0.765	0.641	0.771	0.750	0.756	0.754	0.765	<b>0.775</b>	0.784/0.813 $\dagger$
	$E_\phi \uparrow$	0.753	0.761	0.753	0.777	0.780	0.728	0.785	0.774	0.771	0.727	<b>0.806</b>	0.794	0.787	0.777	0.795	0.785	0.795/0.820 $\dagger$
	$F_\beta^w \uparrow$	0.607	0.595	0.593	0.622	0.630	0.520	0.644	0.659	0.638	0.527	0.680	0.672	0.659	0.658	0.678	0.673	<b>0.704/0.742</b> $\dagger$
	$MAE \downarrow$	0.143	0.144	0.149	0.130	0.129	0.168	0.119	0.116	0.119	0.169	0.109	0.115	0.119	0.121	0.112	0.111	<b>0.103/0.086</b> $\dagger$
OV	$S_m \uparrow$	0.721	0.700	0.688	0.728	0.745	0.624	0.751	0.762	0.781	0.611	0.761	0.748	0.747	0.752	0.779	0.774	<b>0.784/0.826</b> $\dagger$
	$E_\phi \uparrow$	0.735	0.758	0.748	0.758	0.788	0.697	0.755	0.768	0.770	0.685	0.791	0.783	0.780	0.785	<b>0.800</b>	0.785	0.762/0.809 $\dagger$
	$F_\beta^w \uparrow$	0.637	0.622	0.616	0.671	0.682	0.527	0.701	0.733	0.721	0.529	0.723	0.721	0.697	0.707	<b>0.752</b>	0.723	0.750/0.801 $\dagger$
	$MAE \downarrow$	0.173	0.180	0.184	0.159	0.150	0.216	0.136	0.125	0.127	0.217	0.129	0.134	0.148	0.146	0.119	0.126	<b>0.117/0.089</b> $\dagger$
SC	$S_m \uparrow$	0.768	0.761	0.745	0.756	0.783	0.716	0.799	0.772	0.784	0.724	0.808	0.793	0.807	0.793	0.807	0.809	<b>0.810/0.834</b> $\dagger$
	$E_\phi \uparrow$	0.766	0.767	0.769	0.786	0.799	0.746	0.803	0.816	0.779	0.781	0.825	0.841	0.835	0.812	0.819	0.835	<b>0.836/0.885</b> $\dagger$
	$F_\beta^w \uparrow$	0.608	0.599	0.593	0.611	0.638	0.550	0.677	0.669	0.627	0.594	0.696	0.708	0.695	0.678	0.706	0.691	<b>0.721/0.753</b> $\dagger$
	$MAE \downarrow$	0.098	0.098	0.101	0.100	0.090	0.114	0.081	0.087	0.093	0.110	0.076	0.080	<b>0.075</b>	0.083	0.078	0.078	0.079/0.059 $\dagger$
SO	$S_m \uparrow$	0.718	0.713	0.703	0.706	0.737	0.682	0.732	0.736	0.748	0.682	0.746	0.745	0.768	0.749	0.755	0.767	<b>0.779/0.816</b> $\dagger$
	$E_\phi \uparrow$	0.715	0.734	0.731	0.733	0.758	0.723	0.758	0.785	0.750	0.748	0.778	<b>0.790</b>	0.789	0.751	0.771	<b>0.790</b>	0.769/0.856 $\dagger$
	$F_\beta^w \uparrow$	0.523	0.524	0.526	0.531	0.561	0.487	0.567	0.602	0.566	0.518	0.596	0.623	0.626	0.594	0.621	0.614	<b>0.643/0.714</b> $\dagger$
	$MAE \downarrow$	0.119	0.109	0.115	0.116	0.099	0.118	0.096	0.092	0.095	0.113	0.089	0.091	0.087	0.098	0.090	<b>0.082</b>	0.087/0.061 $\dagger$

In fact, our ICON performs favorably against the existing methods across all datasets in terms of nearly all evaluation metrics. This demonstrates the strong capability of our method to deal with challenging inputs. In addition, we present the precision-recall and F-measure curves in Fig. 5. The solid red lines belong to the proposed method are obviously higher than other curves, which further demonstrates the effectiveness of the proposed model.

#### 4.4.2 Visual Comparison

Fig. 6 provides visual comparisons between our approach and the baseline methods. As can be observed, our method generates more accurate saliency maps in various challenging cases, *e.g.*, long-span object (1<sup>st</sup> row), incomplete clews (2<sup>nd</sup> row), low contrast (3<sup>rd</sup> row), clutter (4<sup>th</sup> row), extremely small object (5<sup>th</sup> row), delicate structure (6<sup>th</sup> row) and big object (7<sup>th</sup> row). Besides, our framework can detect salient targets integrally and noiselessly. The above results demonstrate the accuracy and robustness of the proposed method.

#### 4.4.3 Attribute-Based Analysis

In addition to the most frequently used saliency detection datasets, we also test our model on another challenging SOC dataset [15]. Compared with the previous six SOD datasets, this dataset contains many more complicated scenarios. In addition, the SOC dataset categorizes images according to nine different attributes, including AC (appearance change), BO (big object), CL (clutter), HO heterogeneous object), MB (motion blur), OC (occlusion), OV (out-of-view), SC (shape complexity), and SO (small object).

We record sufficient comparison on Table 3 which reports the comparison results between our ICON and 16 state-of-the-art models, including Amulet [20], DSS [115], NLDF [116], C2SNet [107], SRM [117], R3Net [95], BMPM [94], DGRL [118], PiCANet-R (PiCA-R) [23], RANet [119], AFNet [98], CPD [99], PoolNet [27], EGNet [18], BANet [100] and SCRn [101] in terms of attribute-based performance. For the reason some prediction results of some previous methods are generated from the parameters re-trained on the SOC train set, while the others are generating the predictions using the parameters trained on DUTS, we give the

TABLE 4

Ablation analysis of the proposed ICON SOD method. We first show the results when gradually including the proposed components. The best performances are shown in **bold**. We also report the results under other settings to verify their effectiveness, as shown in rows V to XIII.

ID	Settings	OMRON [12]				HKU-IS [88]				DUTS-TE [86]			
		$S_m$	$E_\xi$	$F_\beta^w$	MAE	$S_m$	$E_\xi$	$F_\beta^w$	MAE	$S_m$	$E_\xi$	$F_\beta^w$	MAE
<b>Gradually Using Proposed Model Components</b>													
I	Baseline	0.832	0.854	0.731	0.064	0.902	0.930	0.866	0.043	0.861	0.870	0.801	0.049
II	+DFA	0.837	0.857	0.740	0.063	0.913	0.939	0.875	0.035	0.879	0.886	0.818	0.044
III	+DFA+ICE	0.844	0.864	0.747	0.059	0.924	0.950	0.896	0.029	0.890	0.897	0.832	0.038
IV	+DFA+ICE+PWV(EM)	<b>0.845</b>	<b>0.866</b>	<b>0.762</b>	<b>0.058</b>	<b>0.925</b>	<b>0.956</b>	<b>0.908</b>	<b>0.027</b>	<b>0.892</b>	<b>0.900</b>	<b>0.839</b>	<b>0.037</b>
<b>Comparing Row III with ICEs Using Different Features Operators</b>													
V	+DFA+ICE(all $\oplus$ )	0.837	0.860	0.732	0.062	0.905	0.936	0.880	0.033	0.882	0.883	0.806	0.041
VI	+DFA+ICE(all $\ominus$ )	0.842	0.863	0.739	0.057	0.916	0.939	0.877	0.031	0.882	0.888	0.821	0.040
VII	+DFA+ICE(all $\otimes$ )	0.836	0.859	0.744	0.059	0.912	0.938	0.870	0.033	0.884	0.879	0.827	0.044
<b>Comparing Row III with Using Other Attention Methods</b>													
VIII	+DFA+SE [79]	0.839	0.857	0.720	0.061	0.909	0.935	0.877	0.034	0.888	0.885	0.831	0.039
IX	+DFA+CBAM [80]	0.842	0.860	0.739	0.058	0.917	0.948	0.891	0.031	0.885	0.891	0.832	0.039
X	+DFA+GCT [81]	0.838	0.855	0.712	0.062	0.901	0.931	0.874	0.033	0.883	0.890	0.821	0.041
<b>Comparing Row IV with Using Different Routing Algorithms</b>													
XI	+DFA+ICE+PWV(DR) [83]	0.844	0.865	0.760	0.058	0.923	0.952	0.902	<b>0.027</b>	0.891	<b>0.900</b>	0.835	0.038
XII	+DFA+ICE+PWV(SR) [120]	0.840	0.859	0.745	0.059	0.918	0.947	0.898	0.029	0.886	0.893	0.831	0.040
<b>Comparing Row IV with Using the BCE Loss Only</b>													
XIII	only $L_{bce}$	0.843	0.863	0.755	0.059	0.921	0.953	0.904	<b>0.027</b>	0.888	0.894	0.837	0.039

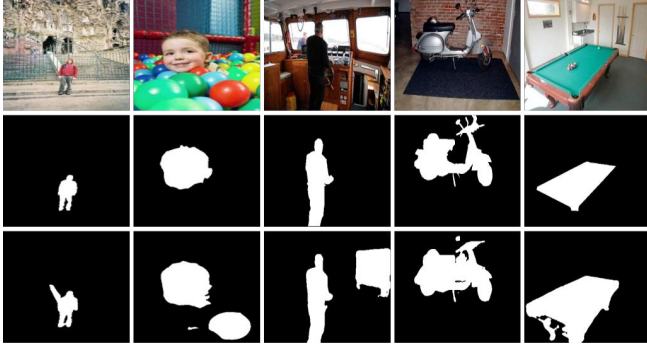


Fig. 8. Failure cases. The first, second and third rows are the input images, ground truths and our predictions, respectively.

results of both above two settings for a fair comparison. According to Table 3, our ICON achieves obvious performance improvement against the existing methods. Particularly, our ICON advances the most of compared items by a large margin (from 1% to 8%).

#### 4.5 Failure Cases

Although the proposed ICON method outperforms other salient object detection algorithms and rarely generates completely incorrect predictions, there are still some false positive results, as shown in Fig. 8. Specifically, in the first column, our model is confused by the white stairs behind the man. The second column shows a baby playing in a ball poll, where our method falsely treats the vivid red ball as one of the salient objects. Further, our method considers the windows as the foreground in the third column. Bricks of the wall are mistakenly predicted as parts of the electromobile in the fourth column. Finally, the whole billiard table is considered to be salient object where the ground truth is only its tabletop.

#### 4.6 Ablation Study

##### 4.6.1 Effectiveness of different components

To demonstrate the effectiveness of different components in our method, we report the quantitative results of the simplified versions of our model. We start from the encoder-decoder baseline (a UNet-like network with skip connections) and progressively extend it with different modules, including DFA, ICE, and PWV. As shown in Table 4, we test the Baseline (I) and DFA (II) elements, which demonstrate an obvious performance promotion. This is reasonable because the DFA has the ability to search for objects with diverse cues. Then we add the ICE module (III), which shows a substantial improvement. Without any doubt, as shown in Table 4 (IV), all components in the proposed model contribute to the final performance.

Further, the feature visualizations are provided in Fig. 10. We observe that the framework progressively extracts better focal regions and achieves better structural integrity for salient objects. Finally, the ICON method captures salient objects with high confidence, demonstrating the reliability and quality of the proposed feature learning method.

For a full evaluation, we also visualize the predicted saliency maps when gradually adding the proposed components in Fig. 9. From (I) to (IV), the *integrity* of predictions are progressively revealed with better quality. These results demonstrate the importance of each component in producing the desired prediction.

##### 4.6.2 Different Operators on ICE

We show the model performance when using different operators on ICE in Table 4 (IV, V, VI, VII). We can see that using group III ( $\otimes$ ,  $\oplus$ ,  $\ominus$ , as shown in Fig. 3 (B)) achieves better performance than using the same operators in feature fusions, such as (V:  $\oplus$   $\oplus$   $\oplus$ , VI:  $\ominus$   $\ominus$   $\ominus$ , VII:  $\otimes$   $\otimes$   $\otimes$ ). We notice that IV achieves superior performance compared with the alternative method using

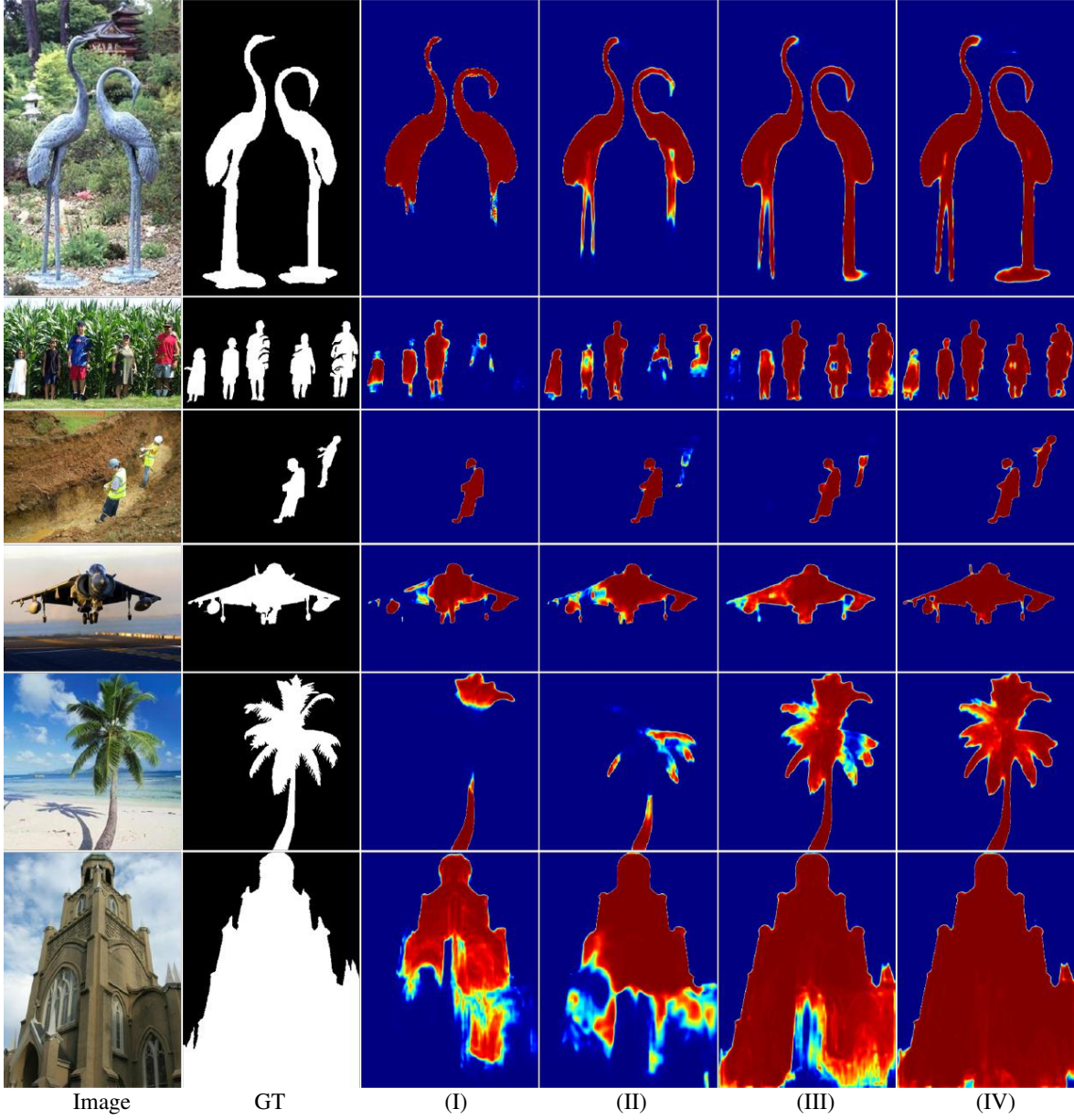


Fig. 9. Visualization of the prediction results when gradually adding various modules. The first columns are the input images. (I)-(IV) denote the corresponding rows of Table 4. We use pseudo colors to emphasize the discrepancy across different prediction results. Best viewed in color.

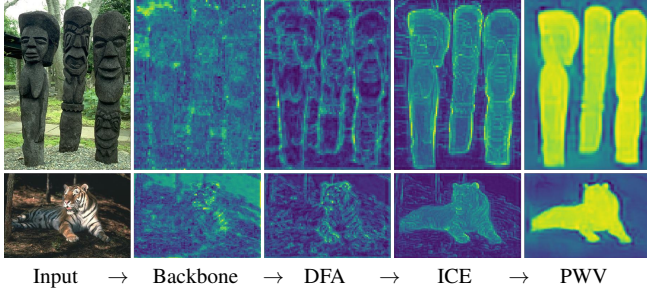


Fig. 10. Visualization results of features learned from different components. Progressively, the method can capture the salient region integrally after transferring through all components.

three identical operations, which demonstrates that enhancing the diversity of features is effective for ICE.

#### 4.6.3 ICE vs. Other Attention Methods

We add an additional control group (IV, VIII, IX, X) to verify the improvement brought by the ICE mechanism. Following IV's setting, we conduct experiments to compare ICE with SE [79], CBAM [80] and GCT [81]. For fair comparison, we perform these experiments using the same training schedule. We observe that the CBAM achieves an acceptable performance and ranks second among these modules. However, the alternative methods using SE and GCT would lead to a noticeable performance drop. A possible explanation is that ICE can strengthen the *integrity* features and highlight potential salient candidates through our carefully designed attention mechanisms.

#### 4.6.4 Evaluation of Different Routing Algorithms

To evaluate the performance of EM routing [32] (IV), we also conduct additional experiments replacing it with the dynamic routing [83] and self-routing [120]. We observe that the alternative

method under setting XI (+PWV(DR)) also achieves reasonable performance, but the other method under setting XII (+PWV(SR)) obtains worse performance when compared with above two settings. A possible reason is that the SR does not have the routing-by-agreement mechanism, which goes against our part-whole verification scheme.

#### 4.6.5 Evaluation of Loss Function

To demonstrate the effectiveness of the loss  $L_{cpr}$ , we conduct another experiment over  $L_{bce}$  based on our ICON architecture. The results reported in (IV and XIII) indicate that after using the loss  $L_{cpr} = L_{iou} + L_{bce}$  in the training process, our model can significantly improve the saliency detection performance across all metrics.

## 5 CONCLUSION

In this work, we present a novel deep neural network, called ICON (Integrity Cognition Network), to detect salient objects from given image scenes. It is based on the observation that mining integrity features (at both a micro and macro level) can substantially benefit the salient object detection process. Specifically, in this work, three novel network modules are designed: the diverse feature aggregation module, the integrity channel enhancement module, and the part-whole verification module. By integrating these modules, ICON is able to capture diverse features at each feature level and enhance feature channels that highlight the potential integral salient objects, as well as further verify the part-whole agreement between the mined salient object regions. Comprehensive experiments on seven benchmark datasets are conducted. The experimental results demonstrate the contribution of each newly proposed component as well as the superior performance of the proposed ICON.

## ACKNOWLEDGMENTS

The authors would like to thank the anonymous reviewers and editor for their helpful comments on this manuscript.

## REFERENCES

- [1] A. Borji, M.-M. Cheng, H. Jiang, and J. Li, “Salient object detection: A benchmark,” *IEEE Trans. Image Process.*, vol. 24, no. 12, pp. 5706–5722, 2015. 1, 7
- [2] D.-P. Fan, Z. Lin, Z. Zhang, M. Zhu, and M.-M. Cheng, “Rethinking rgb-d salient object detection: Models, data sets, and large-scale benchmarks,” *IEEE Trans. Neural Netw. Learn. Syst.*, 2021. 1, 3
- [3] W. Wang, Q. Lai, H. Fu, J. Shen, and H. Ling, “Salient object detection in the deep learning era: An in-depth survey,” *IEEE Trans. Pattern Anal. Mach. Intell.*, 2021. 1
- [4] D. Zhang, J. Han, L. Zhao, and D. Meng, “Leveraging prior-knowledge for weakly supervised object detection under a collaborative self-paced curriculum learning framework,” *Int. J. Comput. Vis.*, vol. 127, no. 4, pp. 363–380, 2019. 1
- [5] G. Liu and D. Fan, “A model of visual attention for natural image retrieval,” in *International Conference on Information Science and Cloud Computing Companion*, 2013, pp. 728–733. 1
- [6] L. Hoyer, M. Munoz, P. Katiyar, A. Khoreva, and V. Fischer, “Grid saliency for context explanations of semantic segmentation,” in *Adv. Neural Inform. Process. Syst.*, 2019, pp. 6462–6473. 1
- [7] Y. Wei, X. Liang, Y. Chen, X. Shen, M.-M. Cheng, J. Feng, Y. Zhao, and S. Yan, “Stc: A simple to complex framework for weakly-supervised semantic segmentation,” *IEEE Trans. Pattern Anal. Mach. Intell.*, vol. 39, no. 11, pp. 2314–2320, 2016. 1
- [8] Y. Zeng, Y. Zhuge, H. Lu, and L. Zhang, “Joint learning of saliency detection and weakly supervised semantic segmentation,” in *Int. Conf. Comput. Vis.*, 2019, pp. 7223–7233. 1
- [9] W. Wang, J. Shen, R. Yang, and F. Porikli, “Saliency-aware video object segmentation,” *IEEE Trans. Pattern Anal. Mach. Intell.*, vol. 40, no. 1, pp. 20–33, 2017. 1
- [10] M.-M. Cheng, N. J. Mitra, X. Huang, P. H. Torr, and S.-M. Hu, “Global contrast based salient region detection,” *IEEE Trans. Pattern Anal. Mach. Intell.*, vol. 37, no. 3, pp. 569–582, 2014. 1
- [11] L. Itti, C. Koch, and E. Niebur, “A model of saliency-based visual attention for rapid scene analysis,” *IEEE Trans. Pattern Anal. Mach. Intell.*, vol. 20, no. 11, pp. 1254–1259, 1998. 1
- [12] C. Yang, L. Zhang, H. Lu, X. Ruan, and M.-H. Yang, “Saliency detection via graph-based manifold ranking,” in *IEEE Conf. Comput. Vis. Pattern Recog.*, 2013, pp. 3166–3173. 1, 6, 7, 8, 10
- [13] W. Zhu, S. Liang, Y. Wei, and J. Sun, “Saliency optimization from robust background detection,” in *IEEE Conf. Comput. Vis. Pattern Recog.*, 2014, pp. 2814–2821. 1
- [14] H. Jiang, J. Wang, Z. Yuan, Y. Wu, N. Zheng, and S. Li, “Salient object detection: A discriminative regional feature integration approach,” in *IEEE Conf. Comput. Vis. Pattern Recog.*, 2013, pp. 2083–2090. 1
- [15] D.-P. Fan, M.-M. Cheng, J.-J. Liu, S.-H. Gao, Q. Hou, and A. Borji, “Salient objects in clutter: Bringing salient object detection to the foreground,” in *Eur. Conf. Comput. Vis.*, 2018, pp. 186–202. 1, 6, 7, 9
- [16] A. Borji, M.-M. Cheng, Q. Hou, H. Jiang, and J. Li, “Salient object detection: A survey,” *Comput. Vis. Media*, pp. 1–34, 2014. 1
- [17] J. Han, D. Zhang, G. Cheng, N. Liu, and D. Xu, “Advanced deep-learning techniques for salient and category-specific object detection: a survey,” *IEEE Signal Process. Mag.*, vol. 35, no. 1, pp. 84–100, 2018. 1
- [18] J.-X. Zhao, J.-J. Liu, D.-P. Fan, Y. Cao, J. Yang, and M.-M. Cheng, “EGNet: Edge guidance network for salient object detection,” in *Int. Conf. Comput. Vis.*, 2019, pp. 8779–8788. 1, 7, 8, 9
- [19] Y. Pang, X. Zhao, L. Zhang, and H. Lu, “Multi-scale interactive network for salient object detection,” in *IEEE Conf. Comput. Vis. Pattern Recog.*, 2020, pp. 9413–9422. 1, 7, 8
- [20] P. Zhang, D. Wang, H. Lu, H. Wang, and X. Ruan, “Amulet: Aggregating multi-level convolutional features for salient object detection,” in *Int. Conf. Comput. Vis.*, 2017, pp. 202–211. 1, 7, 9
- [21] Z. Luo, A. Mishra, A. Achkar, J. Eichel, S. Li, and P. Jodoin, “Non-local deep features for salient object detection,” in *IEEE Conf. Comput. Vis. Pattern Recog.*, 2017, pp. 6593–6601. 2
- [22] T. Zhao and X. Wu, “Pyramid feature attention network for saliency detection,” in *IEEE Conf. Comput. Vis. Pattern Recog.*, 2019, pp. 3085–3094. 2
- [23] N. Liu, J. Han, and M.-H. Yang, “PiCANet: Learning pixel-wise contextual attention for saliency detection,” in *IEEE Conf. Comput. Vis. Pattern Recog.*, 2018, pp. 3089–3098. 2, 7, 8, 9
- [24] ———, “Picanet: Pixel-wise contextual attention learning for accurate saliency detection,” *IEEE Trans. Image Process.*, vol. 29, pp. 6438–6451, 2020. 2
- [25] W. Wang, J. Shen, M.-M. Cheng, and L. Shao, “An iterative and cooperative top-down and bottom-up inference network for salient object detection,” in *IEEE Conf. Comput. Vis. Pattern Recog.*, 2019, pp. 5968–5977. 2
- [26] X. Zhao, Y. Pang, L. Zhang, H. Lu, and L. Zhang, “Suppress and balance: A simple gated network for salient object detection,” in *Eur. Conf. Comput. Vis.*, 2020, pp. 35–51. 2
- [27] J.-J. Liu, Q. Hou, M.-M. Cheng, J. Feng, and J. Jiang, “A simple pooling-based design for real-time salient object detection,” in *IEEE Conf. Comput. Vis. Pattern Recog.*, 2019, pp. 3917–3926. 2, 7, 8, 9
- [28] J. Wei, S. Wang, Z. Wu, C. Su, Q. Huang, and Q. Tian, “Label decoupling framework for salient object detection,” in *IEEE Conf. Comput. Vis. Pattern Recog.*, 2020, pp. 13 025–13 034. 2
- [29] R. Wu, M. Feng, W. Guan, D. Wang, H. Lu, and E. Ding, “A mutual learning method for salient object detection with intertwined multi-supervision,” in *IEEE Conf. Comput. Vis. Pattern Recog.*, 2019, pp. 8150–8159. 2
- [30] M. Amirul Islam, M. Kalash, and N. D. Bruce, “Revisiting salient object detection: Simultaneous detection, ranking, and subitizing of multiple salient objects,” in *IEEE Conf. Comput. Vis. Pattern Recog.*, 2018, pp. 7142–7150. 2
- [31] S. He, J. Jiao, X. Zhang, G. Han, and R. W. H. Lau, “Delving into salient object subitizing and detection,” in *Int. Conf. Comput. Vis.*, 2017, pp. 1059–1067. 2
- [32] G. E. Hinton, S. Sabour, and N. Frosst, “Matrix capsules with em routing,” in *Int. Conf. Learn. Represent.*, 2018. 2, 5, 11
- [33] S.-H. Gao, Y.-Q. Tan, M.-M. Cheng, C. Lu, Y. Chen, and S. Yan, “Highly efficient salient object detection with 100k parameters,” in *Eur. Conf. Comput. Vis.*, 2020, pp. 702–721. 2

[34] Y. Xu, D. Xu, X. Hong, W. Ouyang, R. Ji, M. Xu, and G. Zhao, “Structured modeling of joint deep feature and prediction refinement for salient object detection,” in *Int. Conf. Comput. Vis.*, 2019, pp. 3789–3798. 2

[35] Y. Zeng, P. Zhang, J. Zhang, Z. Lin, and H. Lu, “Towards High-Resolution Salient Object Detection,” in *Int. Conf. Comput. Vis.*, 2019, pp. 7234–7243. 2, 3, 7

[36] K. Zhao, S. Gao, W. Wang, and M.-M. Cheng, “Optimizing the f-measure for threshold-free salient object detection,” in *Int. Conf. Comput. Vis.*, 2019, pp. 8849–8857. 2

[37] Y. Zeng, H. Lu, L. Zhang, M. Feng, and A. Borji, “Learning to promote saliency detectors,” in *IEEE Conf. Comput. Vis. Pattern Recog.*, 2018, pp. 1644–1653. 2

[38] W. Wang, J. Shen, X. Dong, and A. Borji, “Salient object detection driven by fixation prediction,” in *IEEE Conf. Comput. Vis. Pattern Recog.*, 2018, pp. 1711–1720. 2

[39] L. Zhang, J. Zhang, Z. Lin, H. Lu, and Y. He, “Capsal: Leveraging captioning to boost semantics for salient object detection,” in *IEEE Conf. Comput. Vis. Pattern Recog.*, 2019, pp. 6024–6033. 2

[40] X. Hu, L. Zhu, J. Qin, C.-W. Fu, and P.-A. Heng, “Recurrently aggregating deep features for salient object detection,” in *AAAI Conf. Art. Intell.*, vol. 32, no. 1, 2018. 2

[41] L. Wang, L. Wang, H. Lu, P. Zhang, and X. Ruan, “Salient object detection with recurrent fully convolutional networks,” *IEEE Trans. Pattern Anal. Mach. Intell.*, vol. 41, no. 7, pp. 1734–1746, 2018. 2

[42] P. Zhang, W. Liu, H. Lu, and C. Shen, “Salient object detection with lossless feature reflection and weighted structural loss,” *IEEE Trans. Image Process.*, vol. 28, no. 6, pp. 3048–3060, 2019. 2

[43] G. Li and Y. Yu, “Contrast-oriented deep neural networks for salient object detection,” *IEEE Trans. Neural Netw. Learn. Syst.*, vol. 29, no. 12, pp. 6038–6051, 2018. 2

[44] Y. Zhuge, Y. Zeng, and H. Lu, “Deep embedding features for salient object detection,” in *AAAI Conf. Art. Intell.*, vol. 33, 2019, pp. 9340–9347. 2

[45] W. Wang, J. Shen, and L. Shao, “Video salient object detection via fully convolutional networks,” *IEEE Trans. Image Process.*, vol. 27, no. 1, pp. 38–49, 2018. 3

[46] M. Shokri, A. Harati, and K. Taba, “Salient object detection in video using deep non-local neural networks,” *J. Vis. Commun. Image Represent.*, vol. 68, p. 102769, 2020. 3

[47] S. Ren, C. Han, X. Yang, G. Han, and S. He, “Tenet: Triple excitation network for video salient object detection,” in *Eur. Conf. Comput. Vis.*, 2020, pp. 212–228. 3

[48] Y. Su, W. Wang, J. Liu, P. Jing, and X. Yang, “Ds-net: Dynamic spatiotemporal network for video salient object detection,” *arXiv preprint arXiv:2012.04886*, 2020. 3

[49] H. Song, W. Wang, S. Zhao, J. Shen, and K.-M. Lam, “Pyramid dilated deeper convlstm for video salient object detection,” in *Eur. Conf. Comput. Vis.*, 2018, pp. 715–731. 3

[50] X. Shi, Z. Chen, H. Wang, D.-Y. Yeung, W.-K. Wong, and W.-c. Woo, “Convolutional lstm network: A machine learning approach for precipitation nowcasting,” *Adv. Neural Inform. Process. Syst.*, vol. 28, pp. 802–810, 2015. 3

[51] D.-P. Fan, W. Wang, M.-M. Cheng, and J. Shen, “Shifting more attention to video salient object detection,” in *IEEE Conf. Comput. Vis. Pattern Recog.*, 2019, pp. 8554–8564. 3

[52] D. Zhang, H. Fu, J. Han, A. Borji, and X. Li, “A review of co-saliency detection algorithms: Fundamentals, applications, and challenges,” *ACM Trans. Intell. Syst. Technol.*, vol. 9, no. 4, pp. 1–31, 2018. 3

[53] D. Zhang, J. Han, C. Li, J. Wang, and X. Li, “Detection of co-salient objects by looking deep and wide,” *Int. J. Comput. Vis.*, vol. 120, no. 2, pp. 215–232, 2016. 3

[54] D. Zhang, D. Meng, and J. Han, “Co-saliency detection via a self-paced multiple-instance learning framework,” *IEEE Trans. Pattern Anal. Mach. Intell.*, vol. 39, no. 5, pp. 865–878, 2016. 3

[55] D.-P. Fan, Z. Lin, G.-P. Ji, D. Zhang, H. Fu, and M.-M. Cheng, “Taking a deeper look at co-salient object detection,” in *IEEE Conf. Comput. Vis. Pattern Recog.*, 2020, pp. 2919–2929. 3

[56] B. Jiang, X. Jiang, J. Tang, and B. Luo, “Co-saliency detection via a general optimization model and adaptive graph learning,” *IEEE Trans. Multimedia*, pp. 1–1, 2020. 3

[57] W.-D. Jin, J. Xu, M.-M. Cheng, Y. Zhang, and W. Guo, “Icnet: Intra-saliency correlation network for co-saliency detection,” *Adv. Neural Inform. Process. Syst.*, vol. 33, 2020. 3

[58] D.-P. Fan, T. Li, Z. Lin, G.-P. Ji, D. Zhang, M.-M. Cheng, H. Fu, and J. Shen, “Re-thinking co-salient object detection,” *arXiv preprint arXiv:2007.03380*, 2020. 3

[59] J. Han, H. Chen, N. Liu, C. Yan, and X. Li, “Cnns-based rgb-d saliency detection via cross-view transfer and multiview fusion,” *IEEE Trans. Cybern.*, vol. 48, no. 11, pp. 3171–3183, 2018. 3

[60] J. Zhang, D. P. Fan, Y. Dai, S. Anwar, F. S. Saleh, T. Zhang, and N. Barnes, “Uc-net: Uncertainty inspired rgb-d saliency detection via conditional variational autoencoders,” in *IEEE Conf. Comput. Vis. Pattern Recog.*, 2020, pp. 8579–8588. 3

[61] N. Liu, N. Zhang, and J. Han, “Learning selective self-mutual attention for rgb-d saliency detection,” in *IEEE Conf. Comput. Vis. Pattern Recog.*, 2020, pp. 13753–13762. 3

[62] M. Zhang, W. Ren, Y. Piao, Z. Rong, and H. Lu, “Select, supplement and focus for rgb-d saliency detection,” in *IEEE Conf. Comput. Vis. Pattern Recog.*, 2020, pp. 3472–3481. 3

[63] T. Zhou, D.-P. Fan, M.-M. Cheng, J. Shen, and L. Shao, “Rgb-d salient object detection: A survey,” *Comput. Vis. Media*, 2021. 3

[64] Y. Piao, Z. Rong, S. Xu, M. Zhang, and H. Lu, “Dut-lfsaliency: Versatile dataset and light field-to-rgb saliency detection,” *arXiv preprint arXiv:2012.15124*, 2020. 3

[65] Y. Jiang, T. Zhou, G.-P. Ji, K. Fu, Q. Zhao, and D.-P. Fan, “Light field salient object detection: A review and benchmark,” *arXiv preprint arXiv:2010.04968*, 2020. 3

[66] P. Zhang, W. Liu, Y. Zeng, Y. Lei, and H. Lu, “Looking for the detail and context devils: High-resolution salient object detection,” *IEEE Trans. Image Process.*, 2021. 3

[67] D. Zhang, J. Han, and Y. Zhang, “Supervision by fusion: Towards unsupervised learning of deep salient object detector,” in *Int. Conf. Comput. Vis.*, 2017, pp. 4048–4056. 3

[68] D. Zhang, J. Han, Y. Zhang, and D. Xu, “Synthesizing supervision for learning deep saliency network without human annotation,” *IEEE Trans. Pattern Anal. Mach. Intell.*, vol. 42, no. 7, pp. 1755–1769, 2020. 3

[69] T. Nguyen, M. Dax, C. K. Mummadi, N. Ngo, T. H. P. Nguyen, Z. Lou, and T. Brox, “Deepups: Deep robust unsupervised saliency prediction via self-supervision,” in *Adv. Neural Inform. Process. Syst.*, 2019, pp. 204–214. 3

[70] J. Zhang, T. Zhang, Y. Dai, M. Harandi, and R. Hartley, “Deep unsupervised saliency detection: A multiple noisy labeling perspective,” in *IEEE Conf. Comput. Vis. Pattern Recog.*, 2018, pp. 9029–9038. 3

[71] J. Zhang, J. Xie, and N. Barnes, “Learning noise-aware encoder-decoder from noisy labels by alternating back-propagation for saliency detection,” *arXiv preprint arXiv:2007.12211*, 2020. 3

[72] G. Li, Y. Xie, and L. Lin, “Weakly supervised salient object detection using image labels,” in *AAAI Conf. Art. Intell.*, vol. 32, no. 1, 2018. 3

[73] Y. Zeng, Y. Zhuge, H. Lu, L. Zhang, M. Qian, and Y. Yu, “Multi-source weak supervision for saliency detection,” in *IEEE Conf. Comput. Vis. Pattern Recog.*, 2019, pp. 6074–6083. 3

[74] J. Zhang, X. Yu, A. Li, P. Song, B. Liu, and Y. Dai, “Weakly-supervised salient object detection via scribble annotations,” in *IEEE Conf. Comput. Vis. Pattern Recog.*, 2020, pp. 12546–12553. 3

[75] D. Zhang, H. Tian, and J. Han, “Few-cost salient object detection with adversarial-paced learning,” *Adv. Neural Inform. Process. Syst.*, vol. 33, 2020. 3

[76] K. He, X. Zhang, S. Ren, and J. Sun, “Deep residual learning for image recognition,” in *IEEE Conf. Comput. Vis. Pattern Recog.*, 2016, pp. 770–778. 4, 7

[77] X. Ding, Y. Guo, G. Ding, and J. Han, “ACNet: Strengthening the kernel skeletons for powerful cnn via asymmetric convolution blocks,” in *Int. Conf. Comput. Vis.*, 2019, pp. 1911–1920. 4

[78] L.-C. Chen, G. Papandreou, I. Kokkinos, K. Murphy, and A. L. Yuille, “Deeplab: Semantic image segmentation with deep convolutional nets, atrous convolution, and fully connected crfs,” *IEEE Trans. Pattern Anal. Mach. Intell.*, vol. 40, no. 4, pp. 834–848, 2017. 4

[79] J. Hu, L. Shen, and G. Sun, “Squeeze-and-excitation networks,” in *IEEE Conf. Comput. Vis. Pattern Recog.*, 2018, pp. 7132–7141. 10, 11

[80] S. Woo, J. Park, J.-Y. Lee, and I. So Kweon, “Cbam: Convolutional block attention module,” in *Eur. Conf. Comput. Vis.*, 2018, pp. 3–19. 4, 10, 11

[81] Z. Yang, L. Zhu, Y. Wu, and Y. Yang, “Gated channel transformation for visual recognition,” in *IEEE Conf. Comput. Vis. Pattern Recog.*, 2020, pp. 11794–11803. 4, 10, 11

[82] A. Vaswani, N. Shazeer, N. Parmar, J. Uszkoreit, L. Jones, A. N. Gomez, Ł. Kaiser, and I. Polosukhin, “Attention is all you need,” in *Adv. Neural Inform. Process. Syst.*, 2017, pp. 5998–6008. 4

[83] S. Sabour, N. Frosst, and G. E. Hinton, "Dynamic routing between capsules," in *Adv. Neural Inform. Process. Syst.*, 2017, pp. 3856–3866. 5, 10, 11

[84] R. LaLonde and U. Bagci, "Capsules for object segmentation," *arXiv preprint arXiv:1804.04241*, 2018. 5

[85] X. Qin, Z. Zhang, C. Huang, C. Gao, M. Dehghan, and M. Jagersand, "BASNet: Boundary-aware salient object detection," in *IEEE Conf. Comput. Vis. Pattern Recog.*, 2019, pp. 7479–7489. 6, 7, 8

[86] L. Wang, H. Lu, Y. Wang, M. Feng, D. Wang, B. Yin, and X. Ruan, "Learning to detect salient objects with image-level supervision," in *IEEE Conf. Comput. Vis. Pattern Recog.*, 2017, pp. 136–145. 6, 7, 8, 10

[87] Q. Yan, L. Xu, J. Shi, and J. Jia, "Hierarchical saliency detection," in *IEEE Conf. Comput. Vis. Pattern Recog.*, 2013, pp. 1155–1162. 6, 7, 8

[88] G. Li and Y. Yu, "Visual saliency based on multiscale deep features," in *IEEE Conf. Comput. Vis. Pattern Recog.*, 2015, pp. 5455–5463. 6, 7, 8, 10

[89] Y. Li, X. Hou, C. Koch, J. M. Rehg, and A. L. Yuille, "The secrets of salient object segmentation," in *IEEE Conf. Comput. Vis. Pattern Recog.*, 2014, pp. 280–287. 6, 7, 8

[90] V. Movahedi and J. H. Elder, "Design and perceptual validation of performance measures for salient object segmentation," in *IEEE Conf. Comput. Vis. Pattern Recog. Worksh.*, 2010, pp. 49–56. 6, 7, 8

[91] K. He, X. Zhang, S. Ren, and J. Sun, "Delving deep into rectifiers: Surpassing human-level performance on imagenet classification," in *Int. Conf. Comput. Vis.*, 2015, pp. 1026–1034. 7

[92] L. Bottou, "Stochastic gradient descent tricks," in *Neural networks: Tricks of the trade*. Springer, 2012, pp. 421–436. 7

[93] D.-P. Fan, C. Gong, Y. Cao, B. Ren, M.-M. Cheng, and A. Borji, "Enhanced-alignment Measure for Binary Foreground Map Evaluation," in *Int. Joint Conf. Artif. Intell.*, 2018, pp. 698–704. 7, 9

[94] L. Zhang, J. Dai, H. Lu, Y. He, and G. Wang, "A bi-directional message passing model for salient object detection," in *IEEE Conf. Comput. Vis. Pattern Recog.*, 2018, pp. 1741–1750. 7, 8, 9

[95] Z. Deng, X. Hu, L. Zhu, X. Xu, J. Qin, G. Han, and P.-A. Heng, "R3Net: Recurrent residual refinement network for saliency detection," in *Int. Joint Conf. Artif. Intell.*, 2018, pp. 684–690. 7, 8, 9

[96] S. Chen, X. Tan, B. Wang, and X. Hu, "Reverse attention for salient object detection," in *Eur. Conf. Comput. Vis.*, 2018, pp. 234–250. 7, 8

[97] W. Wang, S. Zhao, J. Shen, S. C. Hoi, and A. Borji, "Salient object detection with pyramid attention and salient edges," in *IEEE Conf. Comput. Vis. Pattern Recog.*, 2019, pp. 1448–1457. 7, 8

[98] M. Feng, H. Lu, and E. Ding, "Attentive feedback network for boundary-aware salient object detection," in *IEEE Conf. Comput. Vis. Pattern Recog.*, 2019, pp. 1623–1632. 7, 8, 9

[99] Z. Wu, L. Su, and Q. Huang, "Cascaded partial decoder for fast and accurate salient object detection," in *IEEE Conf. Comput. Vis. Pattern Recog.*, 2019, pp. 3907–3916. 7, 8, 9

[100] J. Su, J. Li, Y. Zhang, C. Xia, and Y. Tian, "Selectivity or invariance: Boundary-aware salient object detection," in *Int. Conf. Comput. Vis.*, 2019, pp. 3799–3808. 7, 8, 9

[101] Z. Wu, L. Su, and Q. Huang, "Stacked Cross Refinement Network for Edge-Aware Salient Object Detection," in *Int. Conf. Comput. Vis.*, 2019, pp. 7264–7273. 7, 8, 9

[102] J. Wei, S. Wang, and Q. Huang, "F<sup>3</sup>net: Fusion, feedback and focus for salient object detection," in *AAAI Conf. Art. Intell.*, vol. 34, no. 07, 2020, pp. 12321–12328. 7, 8

[103] H. Zhou, X. Xie, J.-H. Lai, Z. Chen, and L. Yang, "Interactive two-stream decoder for accurate and fast saliency detection," in *IEEE Conf. Comput. Vis. Pattern Recog.*, 2020, pp. 9141–9150. 7, 8

[104] X. Zhao, Y. Pang, L. Zhang, H. Lu, and L. Zhang, "Suppress and balance: A simple gated network for salient object detection," in *Eur. Conf. Comput. Vis.* Springer, 2020, pp. 35–51. 7, 8

[105] R. Margolin, L. Zelnik-Manor, and A. Tal, "How to evaluate foreground maps?" in *IEEE Conf. Comput. Vis. Pattern Recog.*, 2014, pp. 248–255. 7

[106] G. Li and Y. Yu, "Deep contrast learning for salient object detection," in *IEEE Conf. Comput. Vis. Pattern Recog.*, 2016, pp. 478–487. 7

[107] X. Li, F. Yang, H. Cheng, W. Liu, and D. Shen, "Contour knowledge transfer for salient object detection," in *Eur. Conf. Comput. Vis.*, 2018, pp. 355–370. 7, 9

[108] Y. Liu, Q. Zhang, D. Zhang, and J. Han, "Employing deep part-object relationships for salient object detection," in *Int. Conf. Comput. Vis.*, 2019, pp. 1232–1241. 7

[109] T. Wang, A. Borji, L. Zhang, P. Zhang, and H. Lu, "A stagewise refinement model for detecting salient objects in images," in *Int. Conf. Comput. Vis.*, 2017, pp. 4019–4028. 7

[110] L. Wang, L. Wang, H. Lu, P. Zhang, and X. Ruan, "Saliency detection with recurrent fully convolutional networks," in *Eur. Conf. Comput. Vis.*, 2016, pp. 825–841. 7

[111] Y. Piao, W. Ji, J. Li, M. Zhang, and H. Lu, "Depth-Induced Multi-Scale Recurrent Attention Network for Saliency Detection," in *Int. Conf. Comput. Vis.*, 2019, pp. 7254–7263. 7

[112] G. Li, Y. Xie, L. Lin, and Y. Yu, "Instance-level salient object segmentation," in *IEEE Conf. Comput. Vis. Pattern Recog.*, 2017, pp. 2386–2395. 7

[113] D.-P. Fan, M.-M. Cheng, Y. Liu, T. Li, and A. Borji, "Structure-measure: A new way to evaluate foreground maps," in *Int. Conf. Comput. Vis.*, 2017, pp. 4548–4557. 7

[114] X. Zhang, T. Wang, J. Qi, H. Lu, and G. Wang, "Progressive attention guided recurrent network for salient object detection," in *IEEE Conf. Comput. Vis. Pattern Recog.*, 2018, pp. 714–722. 8

[115] Q. Hou, M.-M. Cheng, X. Hu, A. Borji, Z. Tu, and P. Torr, "Deeply supervised salient object detection with short connections," in *IEEE Conf. Comput. Vis. Pattern Recog.*, 2017, pp. 5300–5309. 9

[116] Z. Luo, A. Mishra, A. Achkar, J. Eichel, S. Li, and P.-M. Jodoin, "Non-local deep features for salient object detection," in *IEEE Conf. Comput. Vis. Pattern Recog.*, 2017, pp. 6593–6601. 9

[117] T. Wang, A. Borji, L. Zhang, P. Zhang, and H. Lu, "A stagewise refinement model for detecting salient objects in images," in *Int. Conf. Comput. Vis.*, 2017, pp. 4039–4048. 9

[118] T. Wang, L. Zhang, S. Wang, H. Lu, G. Yang, X. Ruan, and A. Borji, "Detect globally, refine locally: A novel approach to saliency detection," in *IEEE Conf. Comput. Vis. Pattern Recog.*, 2018, pp. 3127–3135. 9

[119] S. Chen, X. Tan, B. Wang, H. Lu, X. Hu, and Y. Fu, "Reverse attention-based residual network for salient object detection," *IEEE Trans. Image Process.*, vol. 29, pp. 3763–3776, 2020. 9

[120] T. Hahn, M. Pyeon, and G. Kim, "Self-routing capsule networks," in *Adv. Neural Inform. Process. Syst.*, 2019, pp. 7658–7667. 10, 11



**Mingchen Zhuge** received the B.S degree in Internet of Thing engineering from Chinese University of Petroleum in 2018. Currently, he is an M.S. student at Chinese University of Geosciences studying Computer Science. He won the champion of intelligent scheduling group on the 2019 ZTE algorithm competition. And now he is an algorithm intern on Alibaba Group. His main research interests include deep learning based salient object detection, multi-modal representation learning.



**Deng-Ping Fan** received his PhD degree from the Nankai University in 2019. He joined Inception Institute of Artificial Intelligence (IIAI) in 2019. He has published about 25 top journal and conference papers such as CVPR, ICCV, ECCV, etc. His research interests include computer vision and visual attention, especially on RGB salient object detection (SOD), RGB-D SOD, Video SOD, Co-SOD. He won the Best Paper Finalist Award at IEEE CVPR 2019, the Best Paper Award Nominee at IEEE CVPR 2020.



**Nian Liu** is a researcher with Mohamed bin Zayed University of Artificial Intelligence, Abu Dhabi, UAE. He received the Ph.D. degree and the B.S. degree from School of Automation at Northwestern Polytechnical University, in 2020 and 2012, respectively. His research interests include computer vision and machine learning, especially on saliency detection and deep learning.

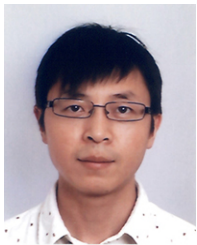


**Dingwen Zhang** received the PhD degree from Northwestern Polytechnical University, China, in 2018. He is a professor with the School of Automation, Northwestern Polytechnical University, China. From 2015 to 2017, he was a visiting scholar at the Robotic Institute, Carnegie Mellon University, Pittsburgh, Pennsylvania. His research interests include computer vision and multimedia processing, especially on saliency detection and weakly supervised learning.



**Dong Xu** is Chair in Computer Engineering at the School of Electrical and Information Engineering, The University of Sydney, Australia. He received the B.Eng. and PhD degrees from University of Science and Technology of China, in 2001 and 2005, respectively. While pursuing the PhD degree, he worked at Microsoft Research Asia and The Chinese University of Hong Kong for more than two years. He also worked as a postdoctoral research scientist at Columbia University from 2006 to 2007 and a faculty member at Nanyang Technological University from 2007 to 2015.

His current research interests include computer vision, multimedia, machine learning and biomedical image analysis. He has published more than 100 papers in IEEE Transactions and top tier conferences including CVPR, ICCV, ECCV, ICML, ACM MM and MICCAI. He is on the editorial boards of IEEE Transactions on Pattern Analysis and Machine Intelligence (T-PAMI), IEEE Transactions on Neural Networks and Learning Systems (T-NNLS) and IEEE Transactions on Circuits and Systems for Video Technology (T-CSVT).



**Ling Shao** is currently the CEO and the Chief Scientist of the Inception Institute of Artificial Intelligence, Abu Dhabi, United Arab Emirates. He is also the Executive Vice President and a Provost of the Mohamed bin Zayed University of Artificial Intelligence. His current research interests include computer vision, machine learning, and medical imaging. Dr. Shao is a fellow of IAPR, IET, and BCS. He is an Associate Editor of the IEEE TRANSACTIONS ON IMAGE PROCESSING, the IEEE TRANSACTIONS ON NEURAL NETWORKS AND LEARNING SYSTEMS, and several other top journals.